Maximum evaporating flux of molecular fluids from a planar liquid surface

Eric Bird and Zhi Liang*
Department of Mechanical Engineering, California State University, Fresno, California 93740, USA

(Received 6 July 2020; accepted 17 September 2020; published 5 October 2020)

In this work, we use the kinetic theory of gases (KTG) to develop a theoretical model to understand the role of internal motions of molecules on the maximum evaporation flux from a planar liquid surface. The kinetic theory is applied to study the evaporation of molecular fluids into a vacuum and predict the dimensionless maximum evaporation flux ($J_{R,\max}$, i.e., the ratio of the maximum evaporation flux to the molar flux emitted from a liquid surface). The key assumptions regarding the velocity distribution function (VDF) of polyatomic molecules in the highly nonequilibrium vapor near the evaporating surface are validated by the VDF obtained directly from molecular dynamics (MD) simulations. Our KTG-based analysis shows that $J_{R,\max}$ is affected by the specific heat ($c_{V,\text{int}}$) associated with internal degrees of freedom of fluid molecules. When the maximum evaporation flux is reached, the isotropic evaporating vapor far from the liquid surface moves at its speed of sound regardless of whether it is a monatomic vapor or polyatomic vapor. To fundamentally understand the evaporation of a molecular fluid into a vacuum, we solve the Boltzmann transport equation (BTE) to obtain the temperature, density, and flow speed distributions in the highly nonequilibrium evaporating vapor flow. Our BTE solutions indicate that there are several universal features of the evaporating vapor when the maximum evaporation flux occurs. In particular, we find that the evaporating vapor flow speed reaches the maximum value of $\sqrt{1.5}$ times the most probable thermal speed in the vapor flow direction at the vacuum boundary, and this maximum value is independent of fluid properties. All theoretical predictions in this work are verified by the MD simulation results of the evaporation of the model liquid Ar and the model liquid *n*-dodecane into a vacuum, and existing experimental data.

DOI: 10.1103/PhysRevE.102.043102

I. INTRODUCTION

Fast evaporation of liquids is a process of great importance to many industrial applications such as evaporative cooling of gas turbines [1], efficient combustion in engines [2], and superfine inkjet printing [3,4]. Accurate prediction of the maximum evaporation flux from a condensed phase is one of the basic problems in the study of fast evaporation processes [5]. The maximum evaporation flux occurs during the evaporation into a vacuum. Due to the importance of this problem, the process of evaporation into a vacuum has been extensively studied in the literature using a variety of theoretical and numerical methods including the kinetic theory of gases (KTG), Boltzmann transport equation (BTE), molecular dynamics (MD) simulation, and direct simulation Monte Carlo (DSMC) method [6–15]. In spite of the extensive work on the process of evaporation into a vacuum in the past decades, most modeling studies only focused on the evaporation of monatomic substances. Such modeling results are suitable for the analysis of experimental data on the evaporation of liquid and solid metals such as Hg and Ag [9,12] into a vacuum. However, whether these modeling results on monatomic fluids can be applied to predict the maximum evaporation flux of more complex fluids such as water and polymers is questionable. To address this question, one must have a fundamental and quantitative understanding of how the internal motions including rotations and vibrations of polyatomic fluid molecules affect the evaporation process and the maximum evaporation flux.

The key issue in the theoretical investigation of the evaporation of molecular fluids into a vacuum is to choose an appropriate velocity distribution function (VDF) for the evaporating vapor molecules. The vapor molecules near the evaporating surface are in highly nonequilibrium states. Therefore, their VDF cannot be accurately described by the Maxwellian equilibrium distribution function [7]. Near the evaporating surface, the kinetic temperature along the evaporation direction is different from that perpendicular to the evaporation direction [7,11]. The temperature anisotropy of evaporating vapor has been observed in experiment [8] and in multiple MD simulations of evaporation of monatomic fluids [11,15–18]. To account for the temperature anisotropy in a monatomic evaporating vapor, one can assign two temperatures to the vapor [7,11]. For a polyatomic evaporating vapor, one also needs to assign a temperature to internal motions in addition to the two temperatures associated with translational motions. It is challenging in experiment to measure the temperatures of translational and internal motions to verify the temperature anisotropy in the evaporating vapor [5]. It is even more challenging to measure the VDF of evaporating vapor molecules to validate the nonequilibrium VDF assumed in the theoretical analysis.

One of the advantages of MD simulations is that MD simulations can readily determine anisotropic temperatures of

*zliang@csufresno.edu

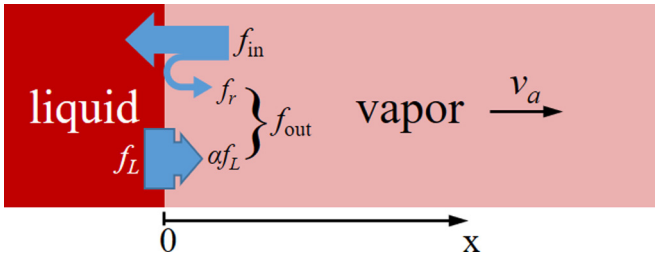

FIG. 1. The schematics diagram of distribution functions of fluid molecules near the evaporating surface.

vapor near the evaporating surface. Additionally, the VDF of evaporating vapor molecules can be directly measured from MD simulations, which allows validating the VDF assumed in the theoretical analysis [11]. With the appropriate VDF, one can use the KTG to formulate boundary conditions for the BTE to fundamentally understand the transport phenomena in the evaporating vapor near a liquid surface, and predict the maximum evaporation flux [6–11]. MD simulations are able to determine fluid properties such as temperature, density, and vapor flow speed near the evaporating surface with high fidelity [5]. Therefore, MD simulation results can be used for testing the accuracy of theoretical predictions of maximum evaporation flux and BTE solutions to the process of evaporation into a vacuum.

In this work, we use the combination of the KTG, BTE, and MD simulations to fundamentally understand the effects of internal motions of molecules on the evaporation of molecular fluids into a vacuum, and evaluate the maximum evaporation flux. In Sec. II, we introduce the key assumptions made in the theoretical analysis of the evaporation of molecular fluids, and apply the KTG to predict the maximum evaporation flux when the vacuum boundary is far from the evaporating surface. In Sec. III, we use MD simulations to validate the key assumptions made in the KTG-based analysis. In Sec. IV, we use the moments method to solve the BTE during the evaporation of a polyatomic vapor into a vacuum, and speculate the general characteristics of the distributions of temperature, density and vapor flow speed along the evaporation direction. In Sec. V we carry out MD simulations to study the evaporation of the model liquid *n*-dodecane and the model liquid Ar into a vacuum to verify the theoretical predictions of the effects of molecular internal motions on the maximum evaporation flux and transport phenomena in the evaporating vapor. Finally, we close with conclusions.

II. MAXIMUM EVAPORATION FLUX PREDICTED BY THE KTG

A. Distribution functions of molecules near the evaporating surface

1. Distribution functions of incoming and outgoing molecules

First, we use the KTG to study the transfer of mass, momentum, and energy across a planar evaporating surface. In the theoretical model, we define the position of liquid surface as the origin of the x coordinate and the evaporation direction as the positive x direction as shown in Fig. 1. To determine the net molar, momentum, and energy flux across an evaporating surface, one needs to evaluate the molar, momentum, and energy fluxes of molecules coming out of the liquid surface and striking the liquid surface. The KTG determines the molar, momentum, and energy fluxes from the distribution functions of fluid molecules.

The molecules that strike the evaporating surface are vapor molecules in the immediate vicinity of the evaporating surface and moving towards the surface. Accordingly, the distribution of incoming molecules is

$$f_{\text{in}} = f(x = 0) \quad (v_x < 0), \tag{1}$$

where f (x=0) is the distribution function of vapor molecules at the vapor side of the liquid-vapor interface, and v_x is the x-component translational velocity of molecules.

The outgoing molecules from an evaporating surface contain two parts. The first part is the molecules that are emitted from the liquid surface and enter the vapor phase. Not all emitted molecules will enter the vapor phase. The fraction α of emitted molecules that change to the vapor phase is known as the mass accommodation coefficient (MAC) [5,19,20]. The second part is the vapor molecules that strike the liquid surface and are reflected from the surface. Accordingly, the distribution function of outgoing molecules from the surface is given by [15,21]

$$f_{\text{out}} = \alpha f_L + f_r \quad (v_x > 0), \tag{2}$$

where f_L is the distribution function of molecules emitted from the liquid surface, and f_r is the distribution function of vapor molecules reflected from the surface. To determine the net evaporation flux, one must choose appropriate distribution functions for molecules emitted from the liquid surface, reflected from the surface, and vapor molecules in the vicinity of the surface.

2. Molecules emitted from the surface

For monatomic fluids, it is commonly assumed that the VDF of molecules emitted from the liquid surface satisfies the Maxwellian distribution with $v_x > 0$ [7,9,11]. To study effects of internal motions on the evaporation of molecular fluids, we add the distribution function of internal motions (f_{int}) as a part of distribution function of polyatomic molecules. For a polyatomic liquid surface at a temperature of T_{L}, we assume that f_L in Eq. (2) is given by

$$f_L(v_x, v_y, v_z, \{v_{\text{int}}\}) = \rho_g(T_L)\left(\frac{m}{2\pi k_B T_L}\right)^{3/2} e^{-m(v_x^2+v_y^2+v_z^2)/2k_B T_L} \times f_{\text{int}@T_L}(\{v_{\text{int}}\})(v_x > 0), \tag{3}$$

where $f_{\text{int}@T_L}$ is f_{int} at a temperature of T_{L}, $\{v_{\text{int}}\}$ are internal variables or quantities, $\rho_g(T_{\text{L}})$ is the saturated vapor density at a temperature of T_{L}, m is the mass of fluid molecule, k_B is the Boltzmann constant, v_y and v_z are translational velocity components of molecules in the y and z directions, respectively. In Eq. (3), f_{int} satisfies

$$\int f_{\text{int}} d(\{v_{\text{int}}\}) = 1, \tag{4a}$$

$$\int E_{\text{int}} f_{\text{int}} d(\{v_{\text{int}}\}) = \bar{E}_{\text{int}}(T_{\text{int}}), \tag{4b}$$

where $T_{\rm int}$ is the temperature of molecular internal motions, $\bar{E}_{\rm int}(T_{\rm int})$ is the expectation value of energy of internal motions (i.e., rotations and vibrations) at a temperature of $T_{\rm int}$. Using the distribution function given in Eq. (3), one can readily obtain the molar flux ($J_L{}^+$), momentum flux ($M_L{}^+$), and energy flux ($E_L{}^+$) of polyatomic molecules emitted from the liquid surface:

$$J_L^+ = \rho_g(T_L)\sqrt{\frac{k_B T_L}{2\pi m}}, \tag{5a}$$

$$M_L^+ = \rho_g(T_L)\frac{k_B T_L}{2m}, \tag{5b}$$

$$E_L^+ = \rho_g(T_L)\left(1+\frac{\bar{E}_{\rm int}(T_L)}{2k_B T_L}\right)2k_B T_L\sqrt{\frac{k_B T_L}{2\pi m}}. \tag{5c}$$

Equations (5a) and (5b) are the same as those for monatomic fluids [7,11]. In the limit of $\bar{E}_{\rm int}=0$, Eq. (5c) is reduced to $E_L{}^+$ for monatomic fluids [7,11] as expected. Hence, the internal motions of molecules only affect the energy flux emitted from the liquid surface.

3. Vapor molecules near the evaporating surface

To evaluate the molar, momentum, and energy fluxes of vapor molecules striking the liquid surface, one needs to know the distribution function of vapor molecules near the evaporating surface. Our previous study on evaporation of monatomic fluids [11] shows that the local VDF of vapor molecules near an evaporating surface can be well approximated by a shifted anisotropic Maxwellian distribution proposed by Crout [7]. In this work, we add the distribution function of internal motions ($f_{\rm int}$) as a part of a distribution function and assume that the local distribution function of polyatomic vapor molecules near the evaporating surface is given by

$$\begin{aligned} f(v_x, v_y, v_z, \{v_{\rm int}\}, x) &= \rho_v(x)\sqrt{\frac{m}{2\pi k_B T_x(x)}} \\ &\times e^{-m[v_x - v_a(x)]^2/2k_B T_x(x)}\left(\frac{m}{2\pi k_B T_y(x)}\right) \\ &\times e^{-m\left(v_y^2+v_z^2\right)/2k_B T_y(x)} f_{{\rm int}@T_{\rm int}(x)}(\{v_{\rm int}\}), \end{aligned} \tag{6}$$

where $\rho_v(x)$ is the local vapor density, $v_a(x)$ is the local average (macroscopic) velocity of vapor, T_x and T_y are temperatures parallel and perpendicular to the vapor flow direction, respectively. In Eq. (6), $f_{\rm int}$ also satisfies Eqs. (4a) and (4b). In this work, we will use MD simulations to determine the VDF of polyatomic vapor molecules near the evaporating surface and validate the distribution function assumption given by Eq. (6).

Using Eq. (6), one can readily obtain the molar (J_v), momentum (M_v), and energy (E_v) fluxes of vapor molecules moving in the positive (+) and negative (–) x directions:

$$J_v^\pm = \rho_v\sqrt{\frac{k_B T_x}{2\pi m}}\Gamma(\pm v_R), \tag{7a}$$

$$M_v^\pm = \rho_v\frac{k_B T_x}{m}\Phi(\pm v_R), \tag{7b}$$

$$E_v^\pm = \rho_v k_B T_x\sqrt{\frac{k_B T_x}{2\pi m}}{\rm E}(\pm v_R), \tag{7c}$$

where v_R is the ratio of the macroscopic speed of vapor v_a to the most probable thermal speed of vapor molecules in the x direction:

$$v_R = v_a/\sqrt{2k_B T_x/m}. \tag{8}$$

In Eq. (7), $\Gamma(v_R)$, $\Phi(v_R)$, and $E(v_R)$ are given by

$$\Gamma(v_R) = e^{-v_R^2} + v_R\sqrt{\pi}[1+{\rm erf}(v_R)], \tag{9a}$$

$$\Phi(v_R) = v_R e^{-v_R^2}/\sqrt{\pi} + \left(\frac{1}{2}+v_R^2\right)[1+{\rm erf}(v_R)], \tag{9b}$$

$$E(v_R) = \sqrt{\pi}\,v_R\Phi(v_R) + (1+T_R+T_{R,{\rm int}})\Gamma(v_R). \tag{9c}$$

In Eq. (9c), $T_R = T_y/T_x$, $T_{R,int} = \bar{E}_{\rm int}(T_{\rm int})/k_B T_x$. The molar, momentum, and energy fluxes of vapor molecules that strike the liquid-vapor interface are $J^-_{v,x=0}$, $M^-_{v,x=0}$, and $E^-_{v,x=0}$, respectively. Comparing Eqs. (7a)–(7c) with those for monatomic fluids, we find that the internal motions of molecules only affect the energy flux of vapor. In the limit of $\bar{E}_{\rm int}=0$, Eq. (7c) is reduced to E_v for monatomic fluids [7,11] as expected.

4. Vapor molecules reflected from the surface

Our recent MD simulation results show that the thermal accommodation coefficient of vapor molecules on their own liquid surfaces is close to unity [22,23], which means the reflection of vapor molecules at their own liquid surface is mostly diffuse, rather than specular. Therefore, most of the vapor molecules would equilibrate with the liquid surface upon reflection. Using the diffuse reflection assumption, f_r in Eq. (2) is given by

$$\begin{aligned} f_r(v_x, v_y, v_z, \{v_{\rm int}\}) &= \rho_r\left(\frac{m}{2\pi k_B T_L}\right)^{3/2} e^{-m\left(v_x^2+v_y^2+v_z^2\right)/2k_B T_L} \\ &\times f_{{\rm int}@T_L}(\{v_{\rm int}\}) \quad (v_x > 0). \end{aligned} \tag{10}$$

Accordingly, the molar, momentum, and energy fluxes of the reflected vapor molecules are given by Eqs. (11a)–(11c), respectively,

$$J_r = \rho_r\sqrt{\frac{k_B T_L}{2\pi m}}, \tag{11a}$$

$$M_r = \rho_r\frac{k_B T_L}{2m}, \tag{11b}$$

$$E_r = \rho_r\left(1+\frac{\bar{E}_{\rm int}(T_L)}{2k_B T_L}\right)2k_B T_L\sqrt{\frac{k_B T_L}{2\pi m}}. \tag{11c}$$

To find ρ_r in Eqs. (10) and (11), we use the mass conservation of vapor molecules striking the liquid surface. Of those molecules that strike the liquid surface, a fraction α (i.e., the MAC), will change to the liquid. The remaining molecules will be reflected without phase change. Hence,

$$J_r = J^-_{v,x=0} - \alpha J^-_{v,x=0}. \tag{12}$$

Substituting Eqs. (7a) and (11a) into Eq. (12), we obtain

$$\rho_r = (1-\alpha)\rho_{v,0}\sqrt{T_{x,0}/T_L}\,\Gamma(-v_{R,0}), \tag{13}$$

where $\rho_{v,0}$, $T_{x,0}$, and $v_{R,0}$ represent ρ_v, T_x, and v_R at $x=0$ (i.e., the vapor side of the evaporating surface), respectively.

B. Vapor properties at the evaporating surface

Based on the distribution functions given in Sec. II A, one can obtain the vapor properties including temperature, density, and macroscopic vapor flow speed at the vapor side of a liquid-vapor interface by applying conservations of mass, momentum, and energy at the interface. In the course of steady-state evaporation, the net molar flux J_{net} across the evaporating surface is equal to J_{net} in the evaporating vapor. Applying the mass conservation at the liquid surface, we have

$$\alpha J_L^+ - J_{v,x=0}^- + J_r = J_{v,x=0}^+ - J_{v,x=0}^-. \tag{14}$$

The left side of Eq. (14) is the J_{net} across the evaporating surface which depends on the molar flux of molecules emitted from the liquid surface ($J_L{}^+$), reflected from the surface (J_r), and striking the surface ($J_{v,x=0}^-$). The right side of Eq. (14) is the J_{net} in the vapor phase at $x = 0$ which is computed from the difference between the molar fluxes of vapor molecules moving in the positive and negative x directions at $x = 0$. Cancelling $J_{v,x=0}^-$ on two sides of Eq. (14) and substituting Eqs. (5a), (7a), and (11a) into Eq. (14), we have

$$\alpha\rho_g(T_L)\sqrt{\frac{k_B T_L}{2\pi m}} + (1-\alpha)\rho_{v,0}\sqrt{\frac{k_B T_{x,0}}{2\pi m}}\Gamma(-v_{R,0}) = \rho_{v,0}\sqrt{\frac{k_B T_{x,0}}{2\pi m}}\Gamma(v_R). \tag{15}$$

Dividing both sides of Eq. (15) by $J_L{}^+$ [i.e., Eq. (5a)], we obtain the following dimensionless equation corresponding to the mass conservation at the evaporating surface:

$$\alpha = \rho_R\sqrt{T_{x,R}}[\Gamma(v_{R,0}) - (1-\alpha)\Gamma(-v_{R,0})], \tag{16}$$

where $\rho_R = \rho_{v,0}/\rho_g(T_L)$ and $T_{x,R} = T_{x,0}/T_L$. The above derivations are similar to those in our previous work for the evaporation of monatomic fluids [11]. The only difference is that we assumed specular reflection of vapor molecules at the liquid surface in our previous work. In this work, we assume the diffuse reflection of vapor molecules at the liquid surface, which is more consistent with recent MD simulation results [22,23].

In a similar manner, we apply the momentum and energy conservation at the evaporating surface and obtain equations similar to Eq. (14):

$$\alpha M_L^+ - M_{v,x=0}^- + M_r = M_{v,x=0}^+ - M_{v,x=0}^-, \tag{17}$$

$$\alpha E_L^+ - E_{v,x=0}^- + E_r = E_{v,x=0}^+ - E_{v,x=0}^-. \tag{18}$$

Rearranging Eqs. (17) and (18), we have

$$\alpha = M_{v,x=0}^+/M_L^+ - M_r/M_L^+ \tag{19}$$

$$\alpha = E_{v,x=0}^+/E_L^+ - E_r/E_L^+. \tag{20}$$

Substituting Eqs. (5b), (7b), and (11b) into Eq. (19), and substituting Eqs. (5c), (7c), and (11c) into Eq. (20), we obtain the following two dimensionless equations corresponding to the momentum conservation and the energy conservation at the liquid surface, respectively:

$$\alpha = \rho_R\sqrt{T_{x,R}}[2\sqrt{T_{x,R}}\Phi(v_{R,0}) - (1-\alpha)\Gamma(-v_{R,0})], \tag{21}$$

$$\alpha = \frac{1}{2}\rho_R\sqrt{T_{x,R}}\left[T_{x,R}E(v_{R,0})\Big/\left(1+\frac{\bar{E}_{\text{int}}(T_L)}{2k_B T_L}\right) - 2(1-\alpha)\Gamma(-v_{R,0})\right]. \tag{22}$$

Applying the conservations of mass, momentum, and energy at the evaporating surface, we obtained three equations, i.e., Eqs. (16), (21), and (22). However, the distribution function of vapor molecules near the evaporating surface, i.e., Eq. (6), contains five unknown parameters: ρ_v, T_x, T_y, T_{int}, and v_a. It is insufficient to use the three conservation equations to determine the five vapor parameters at the liquid surface. To obtain the vapor properties at the liquid surface, we further assume that $T_{\text{int}} \approx T_y$. In this work, we will use MD simulations to calculate T_x, T_y, and T_{int} of evaporating vapor in the course of steady-state evaporation of a molecular fluid into a vacuum, and validate the assumption of $T_{\text{int}} \approx T_y$. With this assumption, the number of unknown parameters in Eq. (6) is reduced to 4. Thus, we can formulate the dimensionless temperatures $T_{x,R}$ and $T_{y,R}$, of vapor and the dimensionless density ρ_R of vapor at the evaporating surface as a function of dimensionless vapor speed v_R at the surface using the three conservation equations:

$$T_{x,R} = \frac{T_{x,0}}{T_L} = \left[\frac{\Gamma(v_{R,0})}{2\Phi(v_{R,0})}\right]^2, \tag{23a}$$

$$T_{y,R} = \frac{T_{y,0}}{T_L} = 1 + \left(1 - \left[\frac{\Gamma(v_{R,0})}{2\Phi(v_{R,0})}\right]^2 - \frac{\Gamma(v_{R,0})\sqrt{\pi}v_{R,0}}{4\Phi(v_{R,0})}\right)\Big/\left(\frac{c_{V,\text{int}}}{k_B}+1\right), \tag{23b}$$

$$\rho_R = \frac{\rho_{v,0}}{\rho_g(T_L)} = \frac{2\alpha\Phi(v_{R,0})}{\Gamma(v_{R,0})[\Gamma(v_{R,0}) - (1-\alpha)\Gamma(-v_{R,0})]}. \tag{23c}$$

The subscript 0 in Eq. (23) indicates that all vapor properties are evaluated at the vapor side of the liquid-vapor interface. In Eq. (23b), $c_{V,\text{int}}$ is the specific heat associated with the internal motions of molecules. Using the dimensionless vapor properties given in Eq. (23), we finally obtain dimensionless molar flux (J_R), which is defined as the ratio of net molar flux from the evaporating surface ($J_{\text{net},x=0}$) to the molar flux emitted from the surface ($J_L{}^+$), as a function of $v_{R,0}$:

$$J_R = \frac{J_{\text{net},x=0}}{J_L^+} = \frac{2\sqrt{\pi}\alpha v_{R,0}}{\Gamma(v_{R,0}) - (1-\alpha)\Gamma(-v_{R,0})}. \tag{24}$$

The derivations of Eqs. (23) and (24) are shown in the Appendix.

In Fig. 2, we plot dimensionless density, temperature, and molar flux of vapor at the evaporating surface as a function of $v_{R,0}$ for different values of α and $c_{V,\text{int}}$. It is evident in Fig. 2 that the extent of nonequilibrium in the evaporating vapor increases with increasing evaporation flux. As $v_{R,0}$ increases, ρ_R falls farther below 1, which means that the density of vapor at the evaporating surface, $\rho_{v,0}$, gets farther below

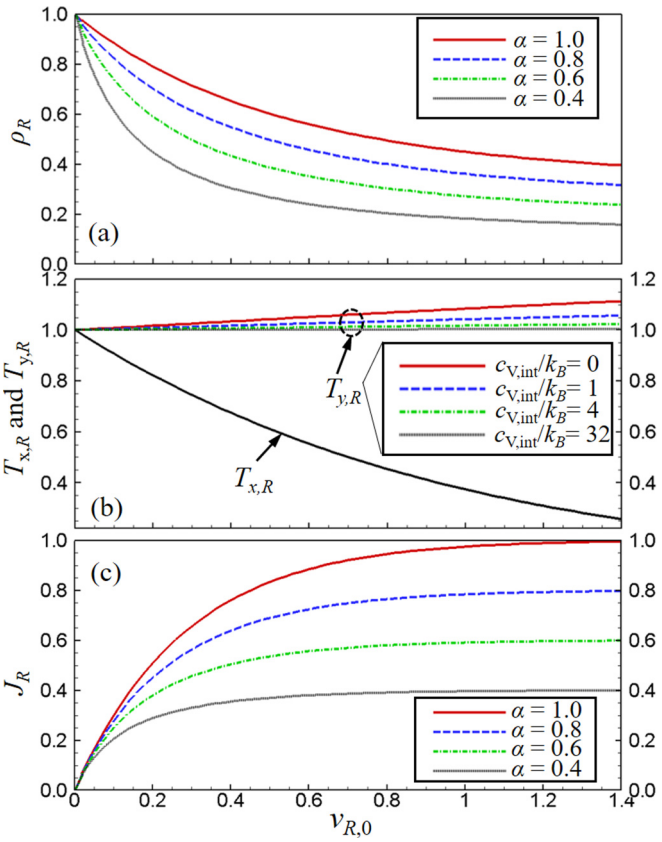

FIG. 2. The dimensionless (a) density, (b) temperature, and (c) molar flux of vapor at the evaporating surface as a function of dimensionless vapor speed at the evaporating surface for different values of α and $c_{V,\mathrm{int}}$.

the saturated vapor density, $\rho_g(T_L)$. When the evaporation vapor speed increases, more microscopic kinetic energy in the direction of evaporation is converted to the macroscopic kinetic energy in the vapor flow. As a result, $T_{x,R}$ gets lower and the difference between $T_{x,R}$ and $T_{y,R}$ gets bigger as $v_{R,0}$ increases. Figure 2(b) also shows that $T_{y,R}$ is $c_{V,\mathrm{int}}$ dependent since we assumed $T_y = T_{\mathrm{int}}$, which implies $T_{y,R}$ is also the dimensionless temperature of internal motions in our model.

The objective of this work is to determine the maximum evaporation flux. For a given α, Fig. 2(c) shows that J_R is a function of $v_{R,0}$ only, and approaches the value of α in the limit of large $v_{R,0}$ as was to be expected [11]. However, this result does not mean the maximum J_R is independent of $c_{V,\mathrm{int}}$. We will show in the next section that the maximum $v_{R,0}$ an evaporating vapor can reach is $c_{V,\mathrm{int}}$ dependent, which in turn makes the maximum J_R dependent on $c_{V,\mathrm{int}}$.

C. Maximum J_R

1. Calculation method

In the last section, we show in Fig. 2(c) that the dimensionless molar flux J_R is an increasing function of dimensionless vapor speed at the evaporating surface $v_{R,0}$. Hence, the maximum J_R is determined by the maximum $v_{R,0}$ an evaporating vapor can reach. To find the maximum $v_{R,0}$, we apply the KTG to study the steady-state evaporation of a liquid into a vacuum where the vacuum boundary is far from the liquid surface.

Using Eqs. (7a)–(7c), one can readily find that the net molar (J_{net}), momentum (M_{net}) and energy (E_{net}) fluxes in the vapor flow are given by

$$J_{\mathrm{net}} = \rho_v v_a, \tag{25a}$$

$$M_{\mathrm{net}} = \rho_v\left(\frac{k_B T_x}{m} + v_a^2\right), \tag{25b}$$

$$E_{\mathrm{net}} = \rho_v v_a\left[\frac{1}{2}mv_a^2 + \frac{3}{2}k_B T_x + k_B T_y + \bar{E}_{\mathrm{int}}(T_y)\right]. \tag{25c}$$

Note that we used the assumption of $T_{\mathrm{int}} = T_y$ in Eq. (25c). We will use MD simulations to validate this assumption in Sec. III. In the course of steady-state evaporation, J_{net}, M_{net}, and E_{net} are constant along the vapor flow direction. Dividing Eq. (25c) by Eq. (25a), therefore, we have

$$\tfrac{1}{2}mv_a^2 + \tfrac{3}{2}k_B T_x + k_B T_y + \bar{E}_{\mathrm{int}}(T_y) = \mathrm{const}. \tag{26}$$

At the evaporating surface, we show in Fig. 2(b) that T_x of vapor is lower than T_y and T_{int} of vapor. When the evaporating vapor molecules move through a long distance, they will have enough time to collide with one another and become isotropic, i.e., $T_x = T_y = T_{\mathrm{int}}$. Applying Eq. (26) to the vapor at the evaporating surface (denoted by subscript 0) and to the isotropic vapor far from the surface (denoted by subscript 1), we have

$$\begin{aligned}&\tfrac{1}{2}mv_{a,0}^2 + \tfrac{3}{2}k_B T_{x,0} + k_B T_{y,0} + \bar{E}_{\mathrm{int}}(T_{y,0})\\ &\quad = \tfrac{1}{2}mv_{a,1}^2 + \tfrac{3}{2}k_B T_1 + k_B T_1 + \bar{E}_{\mathrm{int}}(T_1).\end{aligned} \tag{27}$$

In the isotropic vapor, we only need to assign one temperature, i.e., T_1, to the vapor. In Eq. (27), $\bar{E}_{\mathrm{int}}(T_{y,0}) - \bar{E}_{\mathrm{int}}(T_1) = c_{V,\mathrm{int}}(T_{y,0} - T_1)$, where $c_{V,\mathrm{int}}$ is evaluated at a temperature between $T_{y,0}$ and T_1. Therefore, Eq. (27) can be also written as

$$\begin{aligned}&\tfrac{1}{2}mv_{a,0}^2 + \tfrac{3}{2}k_B T_{x,0} + k_B T_{y,0} + c_{V,\mathrm{int}}T_{y,0}\\ &\quad = \tfrac{1}{2}mv_{a,1}^2 + \tfrac{3}{2}k_B T_1 + k_B T_1 + c_{V,\mathrm{int}}T_1.\end{aligned} \tag{28}$$

Multiplying both sides of Eq. (28) by ${J_{\mathrm{net}}}^2$ and dividing it by ${M_{\mathrm{net}}}^2$, we get

$$\begin{aligned}&\frac{v_{a,0}^2\left(\frac{1}{2}mv_{a,0}^2 + \frac{3}{2}k_B T_{x,0} + k_B T_{y,0} + c_{V,\mathrm{int}}T_{y,0}\right)}{\left(mv_{a,0}^2 + k_B T_{x,0}\right)^2}\\ &\quad = \frac{v_{a,1}^2\left(\frac{1}{2}mv_{a,1}^2 + \frac{3}{2}k_B T_1 + k_B T_1 + c_{V,\mathrm{int}}T_1\right)}{\left(mv_{a,1}^2 + k_B T_1\right)^2}.\end{aligned} \tag{29}$$

Using the definition $v_{R,0} = v_{a,0}/\sqrt{2k_B T_{x,0}/m}$ and $v_{R,1} = v_{a,1}/\sqrt{2k_B T_1/m}$, Eq. (29) is reduced to the following dimensionless equation:

$$\begin{aligned}&\frac{v_{R,0}^2\left[v_{R,0}^2 + \frac{3}{2} + (1 + c_{V,\mathrm{int}}/k_B)T_{R,0}\right]}{\left(v_{R,0}^2 + \frac{1}{2}\right)^2}\\ &\quad = \frac{v_{R,1}^2\left(v_{R,1}^2 + \frac{5}{2} + c_{V,\mathrm{int}}/k_B\right)}{\left(v_{R,1}^2 + \frac{1}{2}\right)^2},\end{aligned} \tag{30}$$

where $T_{R,0} = T_{y,0}/T_{x,0} = T_{y,R}/T_{x,R}$. Noting Eqs. (23a) and (23b) we see that for a given $c_{V,\mathrm{int}}$ the left hand side of Eq. (30) is a function of $v_{R,0}$ only. To find the maximum $v_{R,0}$ (i.e., $v_{R,0,\max}$) from Eq. (30), we denote the left hand side of Eq. (30) as a dimensionless quantity R_0 and the right hand

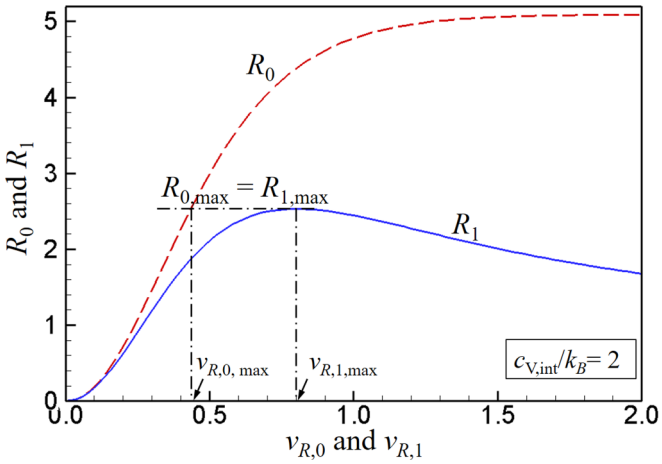

FIG. 3. R_0 vs $v_{R,0}$ and R_1 vs $v_{R,1}$ when $c_{V,\text{int}} = 2k_B$. The solid and dashed lines are R_1 and R_0, respectively. The horizontal dash-dot line shows $R_{0,\max}$ is restricted by $R_{1,\max}$.

side as a dimensionless quantity R_1. In Fig. 3, we show the dependence of R_0 on $v_{R,0}$ and the dependence of R_1 on $v_{R,1}$ when $c_{V,\text{int}} = 2k_B$. For other $c_{V,\text{int}}$ values, the behavior of R_0 and R_1 is similar to that shown in Fig. 3.

If R_0 and R_1 are independent, Fig. 3 shows the maximum value R_0 can reach is higher than that R_1 can reach. However, Eq. (30) requires that $R_0 = R_1$. Therefore, the maximum R_0 value ($R_{0,\max}$) is restricted by the maximum R_1 value ($R_{1,\max}$) as shown in Fig. 3. It can be readily proved that the maximum value of the expression on right hand side of Eq. (30) is given by

$$R_{1,\max} = \frac{\left(\frac{5}{2} + c_{V,\text{int}}/k_B\right)^2}{4 + 2c_{V,\text{int}}/k_B}, \tag{33}$$

which is obtained when

$$v_{R,1,\max}^2 = \frac{\frac{5}{2} + c_{V,\text{int}}/k_B}{3 + 2c_{V,\text{int}}/k_B}. \tag{34}$$

Since $R_0 = R_1$, Eq. (33) also gives $R_{0,\max}$. Figure 3 shows that R_0 is an increasing function of $v_{R,0}$. Therefore, from $R_{0,\max}$ one can find the corresponding $v_{R,0,\max}$. Substituting $v_{R,0,\max}$ into Eq. (24), we obtain the maximum J_R (i.e., $J_{R,\max}$).

The above theoretical analysis is similar to that in Crout's [7] and our previous work [11] on the evaporation of monatomic fluids. In this section, we extend the theoretical method to study the maximum evaporation flux from a molecular liquid. In the analysis, we assumed that the evaporating vapor molecules travel through a long distance and become isotropic before they reach the vacuum boundary. Therefore, the $J_{R,\max}$ predicted by the above-described method corresponds to the J_R in the process of evaporation into a vacuum where the vacuum boundary is many times of molecular mean free paths (MFPs) from the evaporating surface.

Before we show the calculation results in the next section, we summarize the key assumptions we made in the aforementioned KTG-based analysis:

(i) The VDF (f_L) of molecules emitted from the liquid surface satisfies the Maxwellian equilibrium distribution given by Eq. (3).

(ii) The local distribution function of polyatomic vapor molecules near the evaporating surface can be approximated by a shifted anisotropic Maxwellian distribution given by Eq. (6).

(iii) The reflection of vapor molecules at their own liquid surface is diffuse.

(iv) $T_{\text{int}} \approx T_y$ in the evaporating vapor.

(v) The vacuum boundary is many times of molecular MFPs from the evaporating surface.

2. Calculation results

In Table I, we show $v_{R,0,\max}$ and $J_{R,\max}$ calculated by the method described in the last section. Equation (24) indicates that J_R depends on the MAC (α) and $v_{R,0}$. In the last section, we showed $v_{R,0,\max}$ is determined by $R_{0,\max}$, which equals $R_{1,\max}$ and is a function of $c_{V,\text{int}}$ only [see Eq. (33)]. Therefore, $J_{R,\max}$ only depends on two parameters: α and $c_{V,\text{int}}$. The calculation results show that $J_{R,\max}$ is an increasing function of α and a decreasing function of $c_{V,\text{int}}$. The maximum value ($J_{R,\max} = 0.8384$) is obtained when $\alpha = 1$ and $c_{V,\text{int}} = 0$, i.e., the case of evaporation of a monatomic liquid with the MAC equal to 1 into a vacuum. The evaporation of a monatomic substance into a vacuum has been extensively studied by theoretical models [6,7,9–12]. The $J_{R,\max}$'s of monatomic substances reported in these studies are in the range of 0.82–0.85 for $\alpha = 1$, which is consistent with our result. For the evaporation of molecular fluids, our calculation results show that $J_{R,\max}$ decreases with increasing $c_{V,\text{int}}$, which indicates that the maximum evaporation flux is affected by the internal heat capacity of molecules.

Far from the evaporating surface, the evaporating vapor molecules undergo many collisions with one another and become isotropic. To have a better understanding of the process of evaporation into a vacuum, we further calculate the dimensionless temperature ($T_{R,1}$), density ($\rho_{R,1}$), and vapor flow speed ($v_{R,1}$) in the isotropic vapor far from the evaporating surface when the maximum evaporation flux occurs. $T_{R,1}$, which is defined as T_1/T_L, and $\rho_{R,1}$, which is defined as $\rho_{v,1}/\rho_g(T_L)$, are calculated using the method described in the Appendix. It is seen in Table II that $T_{R,1}$ is more strongly affected by $c_{V,\text{int}}$ than $\rho_{R,1}$. Due to molecular collisions in the evaporating vapor, T_x and T_y (or T_{int} since we assume $T_y = T_{\text{int}}$) are approaching each other and eventually equilibrate to T_1. As $c_{V,\text{int}}$ increases, the T_1 will get closer to $T_{y,0}$. In Fig. 2(b), we show that $T_{y,R} = T_{y,0}/T_L$ is always close to unity. Hence, it is reasonable to see that $T_{1,R}$ approaches unity as $c_{V,\text{int}}$ increases.

In Table II, $v_{R,1,\max}$ is directly calculated from Eq. (34). Substituting Eq. (34) into the definition $v_{R,1} = v_{a,1}/\sqrt{2k_BT_1/m}$, we obtain the maximum vapor flow speed in the isotropic vapor far from the evaporating surface is

$$v_{a,1,\max} = \sqrt{\frac{\frac{5}{2}k_B + c_{V,\text{int}}}{\frac{3}{2}k_B + c_{V,\text{int}}}\frac{k_BT_1}{m}}. \tag{35}$$

Assuming the isotropic vapor to be an ideal gas, Eq. (35) becomes

$$v_{a,1,\max} = \sqrt{\frac{c_P}{c_V}\frac{k_BT_1}{m}}, \tag{36}$$

TABLE I. The maximum dimensionless vapor flow speed at the evaporating surface $v_{R,0,\max}$ and the maximum dimensionless evaporation flux $J_{R,\max}$ as a function of $c_{V,\text{int}}$. The $J_{R,\max}$ is obtained in the process of evaporation into a vacuum where the vacuum boundary is far (i.e., many times of molecular mean free paths) from the evaporating surface.

		$J_{R,\max}$									
$c_{V,\text{int}}$ (k_B)	$v_{R,0,\max}$	$\alpha = 1.0$	$\alpha = 0.9$	$\alpha = 0.8$	$\alpha = 0.7$	$\alpha = 0.6$	$\alpha = 0.5$	$\alpha = 0.4$	$\alpha = 0.3$	$\alpha = 0.2$	$\alpha = 0.1$
0	0.508 05	0.8384	0.7670	0.6931	0.6168	0.5378	0.4561	0.3714	0.2836	0.1926	0.0981
1	0.457 46	0.8056	0.7394	0.6705	0.5988	0.5241	0.4462	0.3648	0.2797	0.1908	0.0976
2	0.435 31	0.7892	0.7256	0.6592	0.5897	0.5171	0.4411	0.3614	0.2777	0.1899	0.0974
3	0.422 81	0.7794	0.7173	0.6523	0.5842	0.5129	0.4380	0.3593	0.2765	0.1893	0.0972
4	0.414 75	0.7729	0.7117	0.6477	0.5806	0.5101	0.4359	0.3579	0.2757	0.1889	0.0971
5	0.409 13	0.7682	0.7078	0.6444	0.5779	0.5080	0.4344	0.3569	0.2751	0.1886	0.0971
6	0.404 98	0.7647	0.7048	0.6419	0.5759	0.5065	0.4333	0.3562	0.2746	0.1884	0.0970
7	0.401 79	0.7619	0.7024	0.6400	0.5744	0.5053	0.4324	0.3556	0.2743	0.1882	0.0970
8	0.399 27	0.7597	0.7006	0.6385	0.5731	0.5043	0.4317	0.3551	0.2740	0.1881	0.0969
9	0.397 21	0.7579	0.6991	0.6372	0.5721	0.5035	0.4311	0.3547	0.2738	0.1880	0.0969
10	0.395 51	0.7564	0.6978	0.6361	0.5712	0.5029	0.4307	0.3544	0.2736	0.1879	0.0969
12	0.392 86	0.7541	0.6958	0.6345	0.5699	0.5018	0.4299	0.3538	0.2733	0.1878	0.0968
14	0.390 88	0.7523	0.6943	0.6332	0.5689	0.5010	0.4293	0.3535	0.2730	0.1876	0.0968
16	0.389 36	0.7509	0.6931	0.6323	0.5681	0.5004	0.4289	0.3532	0.2729	0.1876	0.0968
18	0.388 14	0.7498	0.6922	0.6315	0.5675	0.4999	0.4285	0.3529	0.2727	0.1875	0.0968
20	0.387 15	0.7489	0.6914	0.6308	0.5670	0.4995	0.4282	0.3527	0.2726	0.1874	0.0968
24	0.385 62	0.7476	0.6902	0.6298	0.5662	0.4989	0.4278	0.3524	0.2724	0.1873	0.0967
28	0.384 51	0.7465	0.6894	0.6291	0.5656	0.4985	0.4274	0.3522	0.2723	0.1873	0.0967
32	0.383 67	0.7458	0.6887	0.6286	0.5651	0.4981	0.4272	0.3520	0.2722	0.1872	0.0967

where c_P and c_V are the specific heat at constant pressure and constant volume, respectively. The right-hand side of Eq. (36) is the speed of sound of the isotropic vapor. Therefore, Eq. (36) indicates that the maximum evaporation flux occurs when the isotropic vapor far from the evaporating surface moves at its speed of sound. The same result was found for the evaporation of monatomic fluids into a vacuum [7]. Our result shows that it is also true for polyatomic fluids.

The experimental verification of the above theoretical predictions requires a local measurement of fluid properties near the evaporating surface with sufficient accuracy. Our theoretical model predicts that $J_{R,\max}$ depends on the MAC and the specific heat. Although specific heat can be accurately

TABLE II. The dimensionless temperature $T_{R,1}$, vapor flow speed $v_{R,1}$, and density $\rho_{R,1}$ in the isotropic vapor far from the evaporating surface as a function of $c_{V,\text{int}}$ in the process of evaporation into a vacuum where the vacuum boundary is far from the evaporating surface.

			$\rho_{R,1}$									
$c_{V,\text{int}}$ (k_B)	$T_{R,1}$	$v_{R,1.\max}$	$\alpha = 1.0$	$\alpha = 0.9$	$\alpha = 0.8$	$\alpha = 0.7$	$\alpha = 0.6$	$\alpha = 0.5$	$\alpha = 0.4$	$\alpha = 0.3$	$\alpha = 0.2$	$\alpha = 0.1$
0	0.633	0.913	0.326	0.298	0.269	0.240	0.209	0.177	0.144	0.110	0.0748	0.0381
1	0.745	0.837	0.315	0.289	0.262	0.234	0.205	0.174	0.143	0.109	0.0745	0.0381
2	0.805	0.802	0.310	0.285	0.259	0.231	0.203	0.173	0.142	0.109	0.0745	0.0382
3	0.842	0.782	0.307	0.282	0.257	0.230	0.202	0.172	0.141	0.109	0.0745	0.0383
4	0.867	0.769	0.305	0.281	0.255	0.229	0.201	0.172	0.141	0.109	0.0745	0.0383
5	0.885	0.760	0.303	0.279	0.254	0.228	0.201	0.171	0.141	0.109	0.0745	0.0383
6	0.899	0.753	0.302	0.279	0.254	0.228	0.200	0.171	0.141	0.109	0.0745	0.0383
7	0.910	0.748	0.301	0.278	0.253	0.227	0.200	0.171	0.141	0.109	0.0745	0.0384
8	0.919	0.743	0.301	0.277	0.253	0.227	0.200	0.171	0.141	0.108	0.0745	0.0384
9	0.926	0.740	0.300	0.277	0.252	0.227	0.199	0.171	0.141	0.108	0.0745	0.0384
10	0.932	0.737	0.300	0.277	0.252	0.226	0.199	0.171	0.140	0.108	0.0745	0.0384
12	0.942	0.733	0.299	0.276	0.252	0.226	0.199	0.171	0.140	0.108	0.0745	0.0384
14	0.949	0.730	0.299	0.276	0.251	0.226	0.199	0.170	0.140	0.108	0.0745	0.0384
16	0.954	0.727	0.298	0.275	0.251	0.226	0.199	0.170	0.140	0.108	0.0745	0.0384
18	0.959	0.725	0.298	0.275	0.251	0.225	0.199	0.170	0.140	0.108	0.0745	0.0385
20	0.963	0.723	0.298	0.275	0.251	0.225	0.199	0.170	0.140	0.108	0.0745	0.0385
24	0.968	0.721	0.297	0.275	0.250	0.225	0.198	0.170	0.140	0.108	0.0745	0.0385
28	0.972	0.719	0.297	0.274	0.250	0.225	0.198	0.170	0.140	0.108	0.0745	0.0385
32	0.976	0.718	0.297	0.274	0.250	0.225	0.198	0.170	0.140	0.108	0.0745	0.0385

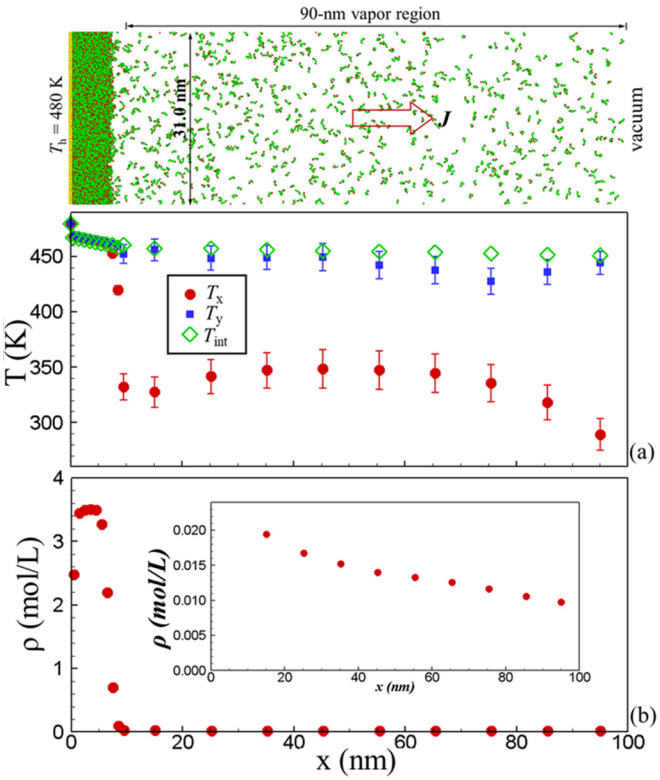

FIG. 4. Top panel: A snapshot of the model system at the end of the MD simulation of evaporation into a vacuum. The temperature of the Au plate is fixed at 480 K. The yellow, red, and green dots in the snapshot represent Au atom and CH_3 and CH_2 pseudoatoms, respectively. Bottom panels: Steady-state (a) temperature (T_x, T_y, and T_{int}), and (b) density profiles. The inset in (b) shows the density profile in the vapor region.

measured in experiment, accurate measurement of the MAC remains challenging in experiment [5]. Without the accurate values of MAC, it is difficult to test the accuracy of our theoretical predictions by experiment. One way to mitigate the experimental challenges is to use MD simulations. MD simulations can determine the microscopic details of fluid molecules near the evaporating surface and evaluate fluid properties including the MAC with a high accuracy. In the following sections, we will use MD simulations to validate the key assumptions in the theoretical model and verify our theoretical predictions.

III. MD SIMULATION OF EVAPORATION INTO A VACUUM

A. MD model

Using MD simulations, we study the evaporation of a model *n*-dodecane into a vacuum. As depicted in Fig. 4, the typical model system consists of a liquid *n*-dodecane thin film on a solid Au slab. The Au slab is formed by three fcc (100) oriented Au atomic layers with a cross section area of 31.0 nm by 31.0 nm. The initial thickness of the liquid layer on the Au surface is approximately 10 nm. The vacuum boundary is 100 nm from the Au surface. The region from $x = 10$–100 nm is defined as the vapor region as shown in Fig. 4. In MD simulations, periodic boundary conditions (PBCs) are applied in the y and z directions, and atoms in the leftmost Au layers are fixed to prevent drifting of the model system.

The united-atom (UA) model is used to model the intra- and intermolecular interactions of *n*-dodecane molecules [24]. For bonded interactions within a *n*-dodecane molecule, we use the Khare *et al.* potential [25,26] to model the two-body bond stretching, the van der Ploeg and Berendsen potential [27] to model the three-body bond bending, and the Jorgensen potential [28] to model the four-body torsion. The nonbonded interactions between any two pseudoatoms that belong to the same molecule but are separated by more than three bonds are modelled by Lennard-Jones (LJ) potential with parameters proposed by Smit *et al.* [29]. Smit *et al.*'s LJ potential is also used to model the interactions between pseudoatoms belonging to different molecules. The Lorentz-Berthelot (LB) mixing rule [30] is employed to determine the LJ parameters for interactions between CH_3 and CH_2 pseudoatoms. The cutoff distance for all LJ interactions is 13.8 Å [24,29]. For Au-Au interactions, we use the embedded-atom-method (EAM) potential [31]. The nonbonded interactions between Au and pseudoatoms in *n*-dodecane are also described by the LJ potential with parameters taken from universal force field (UFF) [32] and calculated by the LB mixing rule. The same cutoff distance of 13.8 Å is used for the LJ interactions between Au and *n*-dodecane.

The above-described MD model has been successfully used to study thermal transport across the liquid-vapor interface of *n*-dodecane in our previous work [23]. The temperature-dependent saturated vapor density $\rho_g(T_L)$ and the MAC $\alpha(T_L)$ of the model *n*-dodecane have been determined by MD simulations in our previous work [23]. In this work, we will use the $\rho_g(T_L)$ and $\alpha(T_L)$ obtained from previous work in the calculation. For the UA model used in this work, each *n*-dodecane molecule contains 12 pseudoatoms. Since the classical MD simulation does not take into account the quantum effects in molecular vibrations, $c_{V,\text{int}}$ of the model *n*-dodecane molecule is equal to $31.5k_B$ in this work.

B. MD simulation details

In all MD simulations, we use a velocity Verlet algorithm with multiple time steps [28] to integrate the equations of motions. A time step size of 1 fs is used for bond stretching; 2 fs is used for bond bending and torsion; 4 fs is used for all other interactions.

To study the steady-state evaporation of the model *n*-dodecane into a vacuum, we maintain the Au plate at $T_h =$ 480 K by velocity rescaling at each time step, and remove *n*-dodecane molecules from the model system once the center of mass of the molecule is out of the vacuum boundary. Such a nonequilibrium MD simulation is first carried for 4 ns to allow the system to reach quasi-steady-state evaporation, and then, for additional 2.5 ns for data collection and averaging. We consider the simulated process as a quasi-steady-state evaporation process since the liquid-vapor interface moves at a speed more than 150 times lower than the bulk velocity of vapor. In the course of the evaporation process, the thickness of liquid film is large enough to avoid effects of

disjoining pressure on the equilibrium properties of the model *n*-dodecane [23].

To calculate the steady-state temperature and density profiles, we evenly divide the fluid region less than 10 nm from the Au surface into ten bins. In the 90-nm-long vapor region, we evenly divide the region into nine bins. The 10-nm bin width in the vapor region allows us to obtain a good statistics of vapor properties. The steady-state evaporation molar flux is determined by $J_{\rm MD} = \Sigma v_{i,x}/(VN_A)$, where N_A is the Avogadro constant, V and $v_{i,x}$ are the volume and the x-component velocity of n-dodecane molecules in the vapor region, respectively. T_x, T_y, and $T_{\rm int}$ in each bin are determined from the average kinetic energy of the molecular translational motions along the vapor flow direction, perpendicular to the vapor flow direction, and the internal motions of molecules in each bin, respectively. The contribution from the macroscopic velocity is subtracted in the calculation of T_x in each bin. To further improve the accuracy of the simulation results, four independent runs are performed in each case of MD simulations. The uncertainties of the simulation results are determined by analyses of these independent runs.

C. MD simulation results

1. Validation of the assumptions in the KTG-based model

We first use the MD simulation results to validate the key assumptions made in the KTG-based analysis. In Sec. II, we assigned three temperatures, i.e., T_x, T_y, and $T_{\rm int}$, to the evaporating vapor and assumed $T_y \approx T_{\rm int}$. It is shown in Fig. 4(a) that T_x in the evaporating vapor is significantly (100–150 K) lower than T_y and $T_{\rm int}$. The lower T_x can be understood as the result of energy conversion from the microscopic kinetic energy in the vapor flow direction to the macroscopic kinetic energy in the evaporating vapor flow during the evaporation process. By contrast, Fig. 4(a) shows that the average difference between T_y and $T_{\rm int}$ in the vapor region is only ~11 K, which is ~2.5% of the average $T_{\rm int}$ in the vapor region. Therefore, our MD simulation results validate that the assumption of $T_y \approx T_{\rm int}$ in our kinetic theory based analysis.

In Sec. II, we assumed that the velocity distribution of evaporating vapor molecules satisfies the Maxwell velocity distribution (MVD) for molecular velocities perpendicular to the vapor flow direction, and satisfies the shifted Maxwell velocity distribution (SMVD) for molecular velocities along the vapor flow direction [see Eq. (6)]. To validate this assumption, we calculate T_x, T_y, and the average vapor flow speed (v_a) in each bin of the vapor region from MD simulations. Using the T_x, T_y, and v_a in each bin, we obtain the corresponding MVD and SMVD, and compare them to the VDFs obtained directly from MD simulations. In Fig. 5, we show that the VDFs obtained directly from MD simulations are in good agreement with the assumed VDFs in bin 1 (i.e., the bin closest to the evaporating surface) and bin 9 (i.e., the bin closest to the vacuum boundary) of the vapor region. The good agreement is also found in all other bins in the vapor region. Therefore, the MD simulation results validate that the VDF of evaporating vapor molecules can be well approximated by Eq. (6).

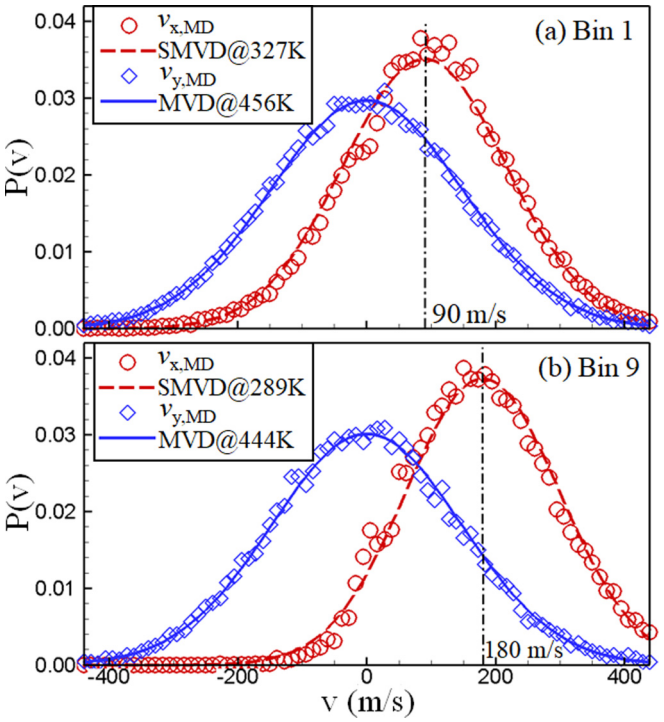

FIG. 5. The VDF of vapor molecules in (a) bin 1 and (b) bin 9 of the vapor region. The red circles and blue diamonds are MD simulation results for the molecular velocity components along and perpendicular to the flow direction, respectively. The solid line is the Maxwell velocity distribution (MVD) of n-dodecane molecules at (a) $T_y = 456$ K and (b) $T_y = 444$ K. The dashed line is the shifted MVD (SMVD) of n-dodecane molecules at (a) $T_x = 327$ K and $v_a = 90$ m/s, and (b) $T_x = 289$ K and $v_a = 180$ m/s.

2. Verification of the KTG prediction

To validate the KTG prediction of $J_{R,\max}$, we first evaluate the liquid surface temperature (T_L) in the MD model. To find the position of the liquid surface and T_L with a high accuracy, we show in Fig. 6 the high spatial-resolution distributions of temperature, density, and molar flux near the evaporating surface obtained from the MD simulation. The MD simulation results show that there is a nanoscopic liquid-vapor interphase layer where the fluid density drops dramatically from the liquid density to the vapor density, and the isotropic temperature profile in the liquid phase splits rapidly into the anisotropic temperature profiles in the vapor flow direction. In Sec. II, we assumed that the temperature at the liquid surface is isotropic [see Eq. (3)]. Accordingly, we define that the liquid surface is located at the rightmost bin where the fluid temperature has not started to diverge. It is shown in Fig. 6 that the liquid surface is located at $x \approx 6.0$ nm and $T_L = 463$ K. For the model n-dodecane at $T_L = 463$ K, our previous work [23] shows $\rho_g = 0.0386$ mol/L and $\alpha = 0.85$. Using $\alpha = 0.85$ and $c_{V,\rm int} = 31.5\,k_B$ in our theoretical model described in Sec. II, we find the KTG prediction $J_{R,\max} = 0.659$.

To compare the KTG prediction with the MD simulation result, we substitute $T_L = 463$ K and $\rho_g(T_L) = 0.0386$ mol/L into Eq. (5a) and obtain $J_L{}^+ = 0.2315$ mol/cm^2 s. It is shown in Fig. 6(b) that the molar flux ($J_{\rm MD}$) increases from 0 in the liquid phase to 0.172 ± 0.04 mol/cm^2 s in the vapor phase

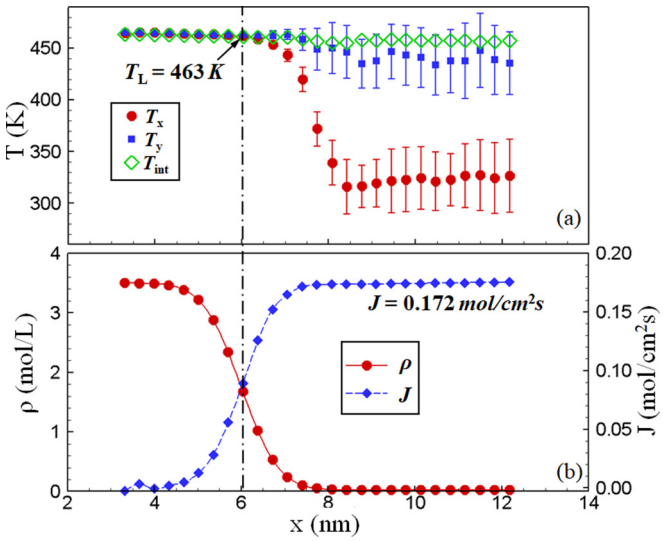

FIG. 6. Steady-state (a) temperature (T_x, T_y, and T_{int}), and (b) density and molar flux profiles near the evaporating surface. The width of each bin is 0.341 nm. The solid line and the dashed line in (b) are used to guide the eye. The vertical dash-dot line indicates the location where the temperature in different directions start to split.

across the interphase layer. The left boundary of the vapor region defined in our MD model is at $x = 10$ nm, which is out of the interphase layer. In the vapor region, J_{MD} is essentially a constant as was to be expected in the course of steady-state evaporation process. Using the definition $J_{R,\text{MD}} = J_{\text{MD}}/J_L^+$, we obtain $J_{R,\text{MD}} = 0.74 \pm 0.02$, which is ~12% higher than the KTG prediction $J_{R,\max} = 0.659$. The deviation between the MD simulation result and the KTG prediction is mainly due to the short distance between the vacuum boundary and the evaporating surface in the MD simulation. In the KTG-based analysis, we assumed that the vacuum boundary is far from the evaporating surface such that the evaporating vapor molecules have sufficient time to collide with one another and become isotropic before they reach the vacuum boundary. However, the MD simulation results in Fig. 4(a) show that even the minimum difference between T_x and T_y in the vapor region is more than 90 K. Therefore, it is inappropriate to use this MD result to directly verify or deny the accuracy of the KTG predictions.

For the model fluid in this study, we will show in the following sections that the vacuum boundary must be several micrometers from the evaporating surface to be considered as sufficiently far. The computational cost for the MD simulation of such a large system is very high. Instead of directly carrying out MD simulation in a very large system, we will vary the distance (L_{vac}) between the vacuum boundary and the evaporating surface from 19 to 194 nm in the MD model and determine $J_{R,\text{MD}}$ for each L_{vac}. Understanding the dependence of $J_{R,\text{MD}}$ on L_{vac} and the transport phenomena in the highly nonequilibrium evaporating vapor requires the treatment from the BTE. Based on the understanding from the BTE, we will extrapolate $J_{R,\text{MD}}$ at the limit of $L_{\text{vac}} \to \infty$ and compare asymptotic value at infinity to the KTG prediction.

IV. BTE SOLUTION TO EVAPORATION INTO A VACUUM

A. BTE

We consider steady-state evaporation of a polyatomic vapor from a planar surface of its own condensed phase. In a steady vapor flow without external forces, the BTE can be written as

$$v_x \frac{\partial f}{\partial x} = Q_{\text{coll}}(f), \tag{37a}$$

where f is the distribution function of vapor molecules, and $Q_{\text{coll}}(f)$ is the collision term accounting for the effect of collisions between vapor molecules. To obtain the form of the collision term, $Q_{\text{coll}}(f)$, we use the well-known approximation made by Bhatnagar, Gross, and Krook (BGK) [33]. The BGK approximation assumes that the molecular collisions force a nonequilibrium distribution function f back to a Maxwellian equilibrium distribution function f_{e} at a rate proportional to the molecular collision frequency. Using the BGK approximation, the BTE is modified to

$$v_x \frac{\partial f}{\partial x} = \frac{(f_e - f)}{\tau}, \tag{37b}$$

where $1/\tau$ is the molecular collision frequency. Using MD simulation results shown in Sec. III, we validated that f of evaporating vapor molecules can be well approximated by Eq. (6). In Sec. V, we will use MD simulations to validate the BGK assumption in the model vapor flow. Since mass, momentum, and energy are conserved during molecular collisions, the local equilibrium distribution function f_{e} should have the form

$$\begin{aligned} &f_e(v_x, v_y, v_z, \{v_{\text{int}}\}, x) \\ &\quad = \rho_v(x)\left(\frac{m}{2\pi k_B T_e(x)}\right)^{3/2} \\ &\qquad \times e^{-m\{[v_x - v_a(x)]^2 + v_y^2 + v_z^2\}/2k_B T_e(x)} f_{\text{int}@T_e(x)}(\{v_{\text{int}}\}), \end{aligned} \tag{38}$$

where $T_{\text{e}} = [T_x/2 + (1 + c_{V,\text{int}}/k_B)T_y]/(1.5 + c_{V,\text{int}}/k_B)$ is obtained based on energy conservation during the molecular collisions in a dilute gas and the assumption of $T_y = T_{\text{int}}$.

The distribution function [i.e., Eq. (6)] of the nonequilibrium evaporating vapor contains four unknown parameters, namely ρ_v, T_x, T_y, and v_a. To understand the variation of these four parameters in the vapor flow direction observed in the MD simulation in Sec. III, we solve the BTE by applying a four-moment method:

$$\begin{aligned} &\int \iiint \phi v_x \frac{\partial f}{\partial x} dv_x dv_y dv_z d(\{v_{\text{int}}\}) \\ &\quad = \int \iiint \phi \frac{(f_e - f)}{\tau} dv_x dv_y dv_z d(\{v_{\text{int}}\}), \end{aligned} \tag{39}$$

where we substitute the function ϕ with four functions, namely 1, $m\vec{v}$, $^1/_2 m\vec{v}^2 + E_{\text{int}}$, and v_x^2, and obtain differential Eqs. (40a)–(40d), respectively,

$$\frac{\partial}{\partial x}(\rho_v v_a) = 0, \tag{40a}$$

$$\frac{\partial}{\partial x}\left[\rho_v\left(k_B T_x + m v_a^2\right)\right] = 0, \tag{40b}$$

$$\frac{\partial}{\partial x}\left\{\rho_v v_a\left[\frac{1}{2}mv_a^2+\frac{3}{2}k_BT_x+k_BT_y+\bar{E}_{\rm int}(T_y)\right]\right\}=0, \quad (40c)$$

$$\frac{\partial}{\partial x}\left[\rho_v v_a\left(v_a^2+\frac{3k_BT_x}{m}\right)\right]=\rho_v\frac{k_B}{m}\frac{T_e-T_x}{\tau}. \quad (40d)$$

In Eq. (40c), we used the assumption of $T_{\rm int}=T_y$. Noting Eqs. (25a)–(25c) we see Eqs. (40a)–(40c) indicate that $J_{\rm net}$, $M_{\rm net}$, and $E_{\rm net}$ remain constant in the vapor flow direction, which is a direct result of mass, momentum, and energy conservation in a steady flow. Rearranging Eqs. (40a)–(40d), we obtain the following four equations which can be used to determine the variation of ρ_v, v_a, T_x, and T_y in the vapor flow direction:

$$\frac{\partial\rho_v}{\partial x}=\frac{T_e-T_x}{\tau}\frac{\rho_v}{v_aT_x\left(2v_R^2-3\right)}, \quad (41a)$$

$$\frac{\partial v_a}{\partial x}=-\frac{T_e-T_x}{\tau}\frac{1}{T_x}\frac{1}{2v_R^2-3}, \quad (41b)$$

$$\frac{\partial T_x}{\partial x}=\frac{T_e-T_x}{\tau}\frac{1}{v_a}\frac{2v_R^2-1}{2v_R^2-3}, \quad (41c)$$

$$\frac{\partial T_y}{\partial x}=-\frac{T_e-T_x}{\tau}\frac{1}{2v_a(c_{V,\rm int}/k_B+1)}. \quad (41d)$$

Four BCs are required to solve the above four coupled differential equations. In Sec. II, we have derived three BCs [i.e., Eqs. (23a)–(23c)] for T_x, T_y, and ρ_v at the evaporating surface. The fourth BC will be specified at the vacuum boundary.

To specify the fourth BC, we analyze the variation of vapor density across the vacuum boundary. On the right side of the vacuum boundary, the vapor density must be zero. However, the vapor density on the left side of the vacuum boundary must be greater than zero. Otherwise, the macroscopic vapor velocity will be infinite according to mass conservation at steady state, which is impossible. The MD simulation result shown in Fig. 4(b) also confirms that the vapor density does not approach zero at the vacuum boundary. This implies that the density gradient at the vacuum boundary becomes infinite. According to Eq. (41a), the infinite density gradient is obtained when $v_R=\sqrt{1.5}$. Therefore, the BC we can apply at the vacuum boundary is $v_R=\sqrt{1.5}$. In our previous study on the evaporation of monatomic fluids [11], we showed that v_R always reaches the maximum value of $\sqrt{1.5}$ at the vacuum boundary. We will verify in Sec. V that such a vacuum BC is also valid for polyatomic fluids.

B. General features of the BTE solution

In our previous work on the evaporation of monatomic fluids [11], we speculated on the general features of the BTE solutions for the evaporating vapor properties. Using a similar analysis, we speculate from Eq. (41) on the general features of the variation of vapor properties along the vapor flow direction in the course of steady-state evaporation of molecular fluids into a vacuum.

(i) From both the KTG model and the MD simulation, we showed that T_e-T_x is always positive in the evaporating vapor. Accordingly, we speculate from Eq. (41d) that T_y will decrease monotonically in the vapor flow direction. Furthermore, Eq. (41d) also indicates that a higher $c_{V,\rm int}$ value will result in a slower decrease of T_y in the vapor flow direction, which will indirectly affect the variation of other fluid properties in the vapor flow direction.

(ii) In Sec. IV A, we speculated that v_R will reach $\sqrt{1.5}$ at the vacuum boundary. The evaporating vapor will accelerate towards the vacuum boundary. Hence, we speculate that v_R will increase in the vapor flow direction, but will always be less than $\sqrt{1.5}$ before the vapor reaches the vacuum boundary. Otherwise, the BTE solution will be divergent at a position before the vacuum boundary, which is impossible. Since $v_R<\sqrt{1.5}$, $2{v_R}^2$–3 in Eq. (41) is always negative. Accordingly, we speculate from Eqs. (41a) and (41b) that ρ_v will decrease monotonically, and v_a will increase monotonically in the flow direction.

(iii) Equation (41c) contains the term $(2{v_R}^2-1)/(2{v_R}^2-3)$. Since $2{v_R}^2-3$ is always negative, we speculate from Eq. (41c) that T_x will increase in the flow direction if ${v_R}^2$ is less than 0.5, and decrease in the flow direction if ${v_R}^2$ is greater than 0.5. If v_R at the evaporating surface, i.e., $v_{R,0}$ is less than $\sqrt{0.5}$, one will see that T_x first increases in the vapor flow direction, reaches the maximum value at the position where $v_R=\sqrt{0.5}$, and then decreases in the vapor flow direction until it reaches the vacuum boundary where $v_R=\sqrt{1.5}$.

In the next section, we will use MD simulations to validate the BGK approximation used in the BTE equation, and verify the aforementioned speculations from the BTE solution.

V. VERIFICATION OF THE BTE SOLUTION

A. Validation of the BGK approximation

To test the accuracy of the BGK approximation for the collision term in the BTE, we carry out an MD simulation to evaluate at which rate molecular collisions will force the nonequilibrium distribution in the model fluid back to a Maxwellian equilibrium distribution. The molecular collision frequency depends on both the temperature and density. In Sec. III, we obtained temperatures (T_x and T_y) and density (ρ_v) in each bin of the vapor region from the MD simulation. To investigate how fast the nonequilibrium vapor will be forced back to equilibrium by molecular collisions, we carry out a separate MD simulation in a cubic simulation box containing 64 800 model *n*-dodecane molecules. The box size is fixed at a value such that the density of *n*-dodecane equals ρ_v. The PBCs are applied in all three directions. We first equilibrate the *n*-dodecane vapor at a temperature of T_y for 1.5 ns such that $T_x=T_y=T_{\rm int}$. After thermal equilibrium, we multiply the v_x of each *n*-dodecane molecule by $\sqrt{T_x/T_y}$ to create a nonequilibrium velocity distribution:

$$f_{\rm ne}(v_x,v_y,v_z,\{v_{\rm int}\},t)=\rho_v\sqrt{\frac{m}{2\pi k_BT_x(t)}}e^{-mv_x^2/2k_BT_x(t)}\left(\frac{m}{2\pi k_BT_y(t)}\right)\times e^{-m\left(v_y^2+v_z^2\right)/2k_BT_y(t)}f_{{\rm int}@T_y(t)}(\{v_{\rm int}\}). \quad (42)$$

Subsequently, we carry out an *NVE* simulation to determine how T_x and T_y vary with time, t, and compare the MD simulation results with the prediction from the BTE solution. Since the PBCs are applied in all three directions in the MD simulation, $f_{\rm ne}$ is spatially independent. In this case, the BTE

becomes

$$\frac{\partial f_{\rm ne}}{\partial t} = \frac{(f_{\rm eq} - f_{\rm ne})}{\tau}, \tag{43}$$

where the equilibrium distribution function in Eq. (43) is given by

$$f_{\rm eq}(v_x, v_y, v_z, \{v_{\rm int}\}) = \rho_v \left(\frac{m}{2\pi k_B T_e}\right)^{3/2} e^{-m(v_x^2+v_y^2+v_z^2)/2k_B T_e} \times f_{{\rm int}@T_e}(\{v_{\rm int}\}). \tag{44}$$

In Eq. (44), $T_{\rm e} = [T_x/2 + (1 + c_{V,{\rm int}}/k_B)T_y]/(1.5 + c_{V,{\rm int}}/k_B)$ according to energy conservation during the molecular collisions in a dilute gas. To solve Eq. (43), we use the same moments method described in Sec. IV A and set $\phi = v_x^2$. Accordingly, we obtain

$$\frac{\partial T_x}{\partial t} = \frac{T_e - T_x}{\tau}. \tag{45}$$

Applying the initial condition $T_x(t = 0) = T_{x,i}$, the solution to Eq. (45) is

$$\ln \frac{T_x(t) - T_e}{T_{x,i} - T_e} = -\frac{t}{\tau}. \tag{46}$$

According to the KTG, the molecular collision frequency $1/\tau$ can be estimated by [34]

$$\frac{1}{\tau} = 4\rho_v \pi d^2 \sqrt{\frac{k_B T_{\rm tr,avg}}{\pi m}}, \tag{47}$$

where d is the kinetic diameter of vapor molecules, and $T_{tr,{\rm avg}} = (T_x + 2T_y)/3$ is the average translational temperature since the collision frequency is mainly affected by the translational motions rather than internal motions of molecules. If the BGK approximation is accurate, we should be able to use Eq. (46) to evaluate the molecular collision frequency $1/\tau$ from the MD simulation results. The calculated $1/\tau$ should be proportional to $\rho_v\sqrt{T_{\rm tr,avg}}$ according to the KTG prediction, i.e., Eq. (47).

In Fig. 7(a), we show the variation of T_x, T_y, and $T_{\rm int}$ with t obtained from MD simulation of the model vapor n-dodecane whose density is $\rho_v = 0.0194\,{\rm mol/L}$ and initial temperatures are $T_{x,i} = 327\,{\rm K}$ and $T_{y,{\rm i}} = 455\,{\rm K}$. The density and temperature are taken from the vapor property in bin 1 (i.e., the leftmost bin) of the vapor region in Fig. 4. It is seen from Fig. 7(a) that T_y is always close to $T_{\rm int}$ during the molecular collision process in the nonequilibrium vapor. This result further validates our assumption of $T_y = T_{\rm int}$ in the theoretical analysis. The inset of Fig. 7(a) shows $\ln\{[T_x(t)–T_{\rm e}]/(T_{x,i}–T_{\rm e})\}$ is proportional to t, which is consistent with the prediction from Eq. (46). The slope of the linear fit gives $1/\tau = 0.0062\,{\rm ps}^{-1}$ for the model fluid with the density and temperature in bin 1. The molecular collision frequency can be also determined from the Einstein-Smoluchowski (ES) equation [35] which relates $1/\tau$ to the self-diffusion coefficient D. To verify the $1/\tau$ value found in Fig. 7(a), we carry out a separate equilibrium MD simulation in a vapor with $\rho_v = 0.0194\,{\rm mol/L}$ and $T = 412.3\,{\rm K}$ ($T_{tr,{\rm avg}}$ in bin 1) to calculate the velocity autocorrelation function and find $D = 4.2 \times 10^{-6}\,{\rm m}^2/{\rm s}$ from the Green-Kubo formula [36]. Accordingly, the ES equation predicts $1/\tau = 0.0061\,{\rm ps}^{-1}$ which is consistent with that found in Fig. 7(a). Using the same method

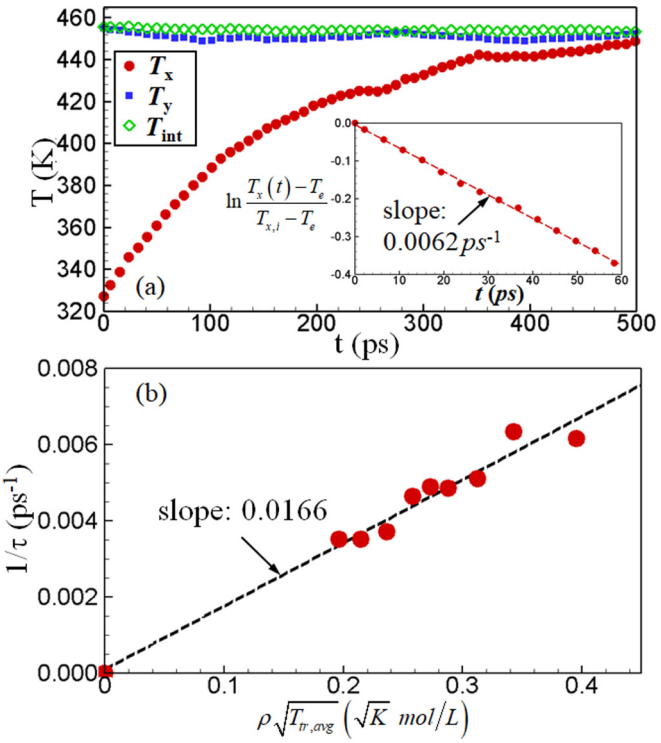

FIG. 7. (a) Variation of T_x, T_y, and $T_{\rm int}$ with t obtained from MD simulation of the model n-dodecane vapor with a density of $\rho_v = 0.0194\,{\rm mol/L}$ and an initial temperature of $T_{x,i} = 327\,{\rm K}$ and $T_{y,{\rm i}} = 455\,{\rm K}$. The inset shows a linear fit of $\ln\{[T_x(t)–T_{\rm e}]/(T_{x,i}–T_{\rm e})\}$ vs t. (b) The dependence of molecular collision frequency, $1/\tau$, on $\rho_v\sqrt{T_{\rm tr,avg}}$ obtained from MD simulations. The dashed line is the linear fit of $1/\tau$ vs $\rho_v\sqrt{T_{\rm tr,avg}}$.

[i.e., Eq. (46)], we find $1/\tau$ for vapor properties in all other bins in the vapor region. The MD data in Fig. 7(b) show that $1/\tau$ is proportional to $\rho_v\sqrt{T_{\rm tr,avg}}$ as was predicted by the KTG. Therefore, the MD simulation results indicate the BGK approximation accurately describes the collision term in the BTE for the model fluid.

If ρ_v and T are in unit of mol/L and K, respectively, we find from Fig. 7(b) that $1/\tau_{MD} = 0.0166\rho_v\sqrt{T_{\rm tr,avg}}\,{\rm ps}^{-1}$. Using this MD simulation result in Eq. (47), we evaluate that the kinetic diameter of the model n-dodecane vapor molecule is 0.74 nm. With the kinetic diameter determined from the MD simulation, we estimate the mean free path of vapor molecules in the vapor region using $\lambda = 1/(\sqrt{2}\pi\rho_v d^2)$ [34]. Figure 4(b) shows that ρ_v reduces from 0.0194 to 0.0098 mol/L in the vapor region. Accordingly, the mean free path of vapor molecules increases from 35 nm at the position near the evaporating surface to 70 nm at the position close to the vacuum boundary. Since the vacuum boundary shown in Fig. 4 is less than 100 nm from the evaporating surface, it is reasonable to see in Fig. 4(a) that the evaporating vapor molecules do not have sufficient time to collide with one another to become isotropic before they reach the vacuum boundary.

B. BTE solution to evaporation of *n*-dodecane

In this section, we solve the BTE by numerical integration of Eq. (41) to study the evaporation of the model n-dodecane

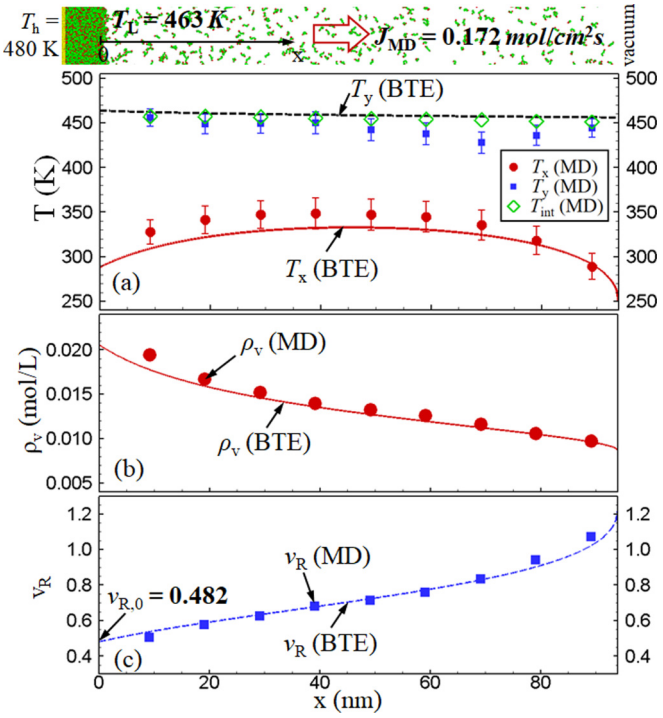

FIG. 8. Top panel: A snapshot of the MD model system for the study of evaporation of n-dodecane at $T_L = 463$ K into a vacuum. The vacuum boundary is ∼94 nm from the evaporating surface. Bottom panels: The (a) temperature, (b) density, and (c) dimensionless macroscopic velocity in the vapor region. The scatters are MD simulation results. The lines are predictions from the BTE.

into a vacuum. An important parameter in Eq. (41) is the molecular collision frequency, $1/\tau$, which depends on the local density and temperature of the evaporating vapor. We will use the relation $1/\tau = 0.0166\rho_v\sqrt{T_{\mathrm{tr,avg}}}\,\mathrm{ps}^{-1}$, found in the last section in the calculation. From the MD simulation results shown in Fig. 6, we found the evaporating surface is located at $x \approx 6.0$ nm and the liquid surface temperature $T_L = 463$ K. Accordingly, the distance between the vacuum boundary and the evaporation surface is $L_{\mathrm{vac}} \approx 94$ nm, and the properties of the model n-dodecane that will be used in the BTE solution are $\rho_g(T_L) = 0.0386$ mol/L, $\alpha(T_L) = 0.85$ [23], and $c_{V,\mathrm{int}} = 31.5\,k_B$.

As discussed in Sec. IV A, the four-moment solution to the BTE requires four BCs. Three of them, i.e., $T_{x,R}$, $T_{y,R}$, and ρ_R, are formulated at the evaporating surface, and the fourth one, i.e., $v_R = \sqrt{1.5}$, is at the vacuum boundary. To impose the BC at the vacuum boundary, we set $x = 0$ at the evaporating surface and apply a shooting method in which we gradually increase the $v_{R,0}$ value until the BTE solution becomes divergent at the vacuum boundary. As shown in Fig. 8(c), when $v_{R,0} = 0.482$, v_R keeps increasing in the vapor flow direction and approaches 1.224 (i.e., $\sim\sqrt{1.5}$) at $x = 94$ nm (i.e., the position of the vacuum boundary in the MD model). A slight increase in $v_{R,0}$ will make the BTE solution divergent at a position before $x = 94$ nm. With $v_{R,0} = 0.482$, therefore, we imposed the four BCs and obtain the corresponding solution to the BTE. Substituting $v_{R,0} = 0.482$ obtained from the BTE solution into Eq. (24), we obtain the BTE prediction $J_{R,\mathrm{BTE}} = 0.72$ in the case of $L_{\mathrm{vac}} \approx 94$ nm. This value agrees with the MD result $J_{R,\mathrm{MD}} = 0.74 \pm 0.02$, which implies that the deviation between $J_{R,\mathrm{MD}}$ and $J_{R,\mathrm{max}}$ predicted by the KTG is mainly caused by the short distance between the vacuum boundary and the vacuum surface.

As shown in Fig. 8, the T_x, T_y, ρ_v, and v_R profiles predicted by the BTE are all in good agreement with the MD simulation results. In particular, the MD simulation results show that v_R indeed approaches 1.224 near the vacuum boundary, and T_x reaches the maximum value at a position between bin 4 ($x = 39$ nm) and bin 5 ($x = 49$ nm) in the evaporating vapor. The v_R value in bins 4 and 5 are 0.68–0.71, respectively. Hence, the MD simulation results indicate the maximum T_x in the evaporating vapor is obtained when v_R falls between 0.68 and 0.71. This verifies the speculation from our BTE solution that the maximum T_x is reached at $v_R = \sqrt{0.5}$ (i.e., ∼0.707).

The good agreement between the BTE speculations and the MD simulation results was also found in our previous study on the evaporation of monatomic vapor into a vacuum [11]. Moreover, the speculations from the BTE are also consistent with the experimental data on the evaporation of iodine into a vacuum [8]. The experimental data also show that the dimensionless vapor flow speed v_R of iodine approaches $\sqrt{1.5}$ at a condensing surface cooled by liquid nitrogen, which is equivalent to the vacuum boundary [11], and the maximum T_x is obtained at $v_R \approx \sqrt{0.5}$ [8]. These results suggest that the BTE speculations described in Sec. IV B are universal, and can be applied to various evaporating vapors regardless of their molecular structures.

C. Dependence of $J_{R,\mathrm{max}}$ on L_{vac}

To verify $J_{R,\mathrm{max}}$ predicted by the KTG in Sec. II, we vary the distance, L_{vac}, between the evaporating surface to the vacuum boundary from 5 to 2000 nm and use the shooting method described in Sec. V B to solve the BTE to find $v_{R,0}$ and $J_{R,\mathrm{BTE}}$ for each L_{vac}. If L_{vac} is less than 200 nm, we verify the BTE solution by directly comparing to MD simulation results. In Fig. 9, we show the MD simulation results and the BTE solution in the case of evaporation of n-dodecane at $T_L = 463$ K into a vacuum with $L_{\mathrm{vac}} = 194$ nm. Similar to the $L_{\mathrm{vac}} = 94$ nm case, the MD simulation results shown in Fig. 9 agree with all of the BTE speculations very well. In particular, the MD simulation results show v_R approaches 1.224 (i.e., $\sqrt{1.5}$) near the vacuum boundary, and the maximum $T_x = 387$ K is obtained in bin 10 (located at $x = 99$ nm) where $v_R = 0.72$ (close to $\sqrt{0.5}$). Since L_{vac} in Fig. 9 is much longer than that in Fig. 8, the evaporating vapor molecules have more time to collide with one another before they reach the vacuum boundary. As a result, the minimum difference between T_y and T_x is reduced from 93 K for $L_{\mathrm{vac}} = 94$ nm to 52 K for $L_{\mathrm{vac}} = 194$ nm. When $L_{\mathrm{vac}} = 194$ nm, the BTE solution shows $v_{R,0} = 0.436$ and $J_{R,\mathrm{BTE}} = 0.69$. $J_{R,\mathrm{BTE}}$ is again consistent with the MD result $J_{R,\mathrm{MD}} = 0.72 \pm 0.02$. Both $v_{R,0}$ and $J_{R,\mathrm{BTE}}$ values in the $L_{\mathrm{vac}} = 194$ nm case are lower than those in the $L_{\mathrm{vac}} = 94$ nm case. This implies both $v_{R,0}$ and $J_{R,\mathrm{BTE}}$ are L_{vac} dependent.

As L_{vac} increases, the outgoing vapor molecules from the evaporating surface will travel a longer distance before they reach the vacuum boundary. As a result, they have a higher

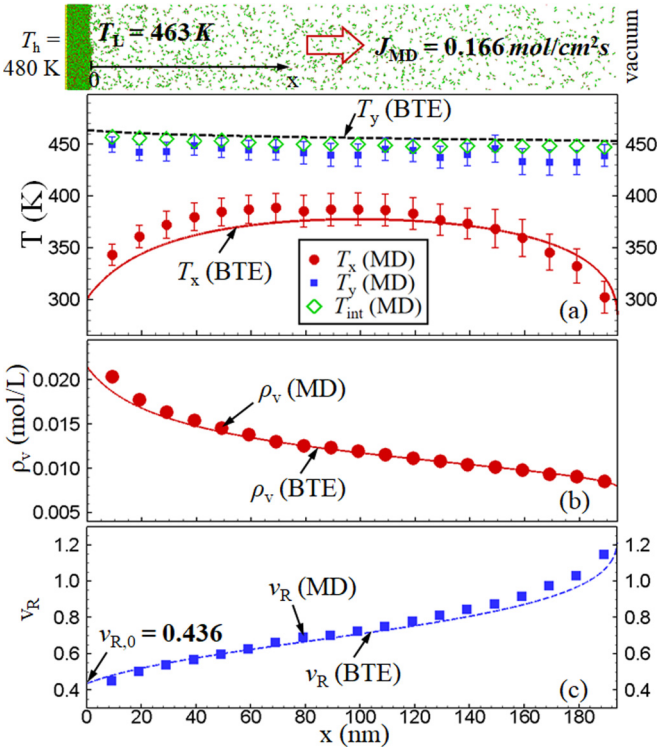

FIG. 9. The same as Fig. 8 except that the distance from the evaporating surface to the vacuum boundary is increased to 194 nm.

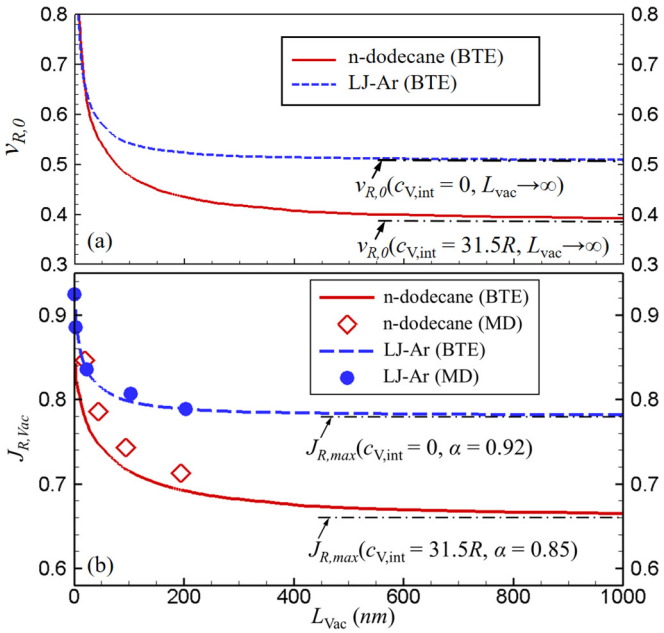

FIG. 10. The BTE predictions of (a) dimensionless vapor flow speed $v_{R,0}$ and (b) dimensionless evaporation flux J_R as functions of L_{vac}. The scatters in (b) are MD simulation results. The dash-dot horizontal lines are the KTG predictions of $v_{R,0}$ and $J_{R,max}$ in the limit of $L_{vac} \to \infty$.

possibility to collide with other vapor molecules, change the moving direction, and return to liquid surface. Hence, it is reasonable to see in Fig. 10 that the BTE predictions of $v_{R,0}$ and $J_{R,BTE}$ are both decreasing functions of L_{vac}. For L_{vac} below 200 nm, we verify the BTE prediction by directly comparing to MD simulation results. In the limit of $L_{vac} \to \infty$, our KTG-based analysis predicts $v_{R,0} = 0.384$ and $J_{R,max} = 0.659$ for the model *n*-dodecane with $\alpha = 0.85$ and $c_{V,int} = 31.5\,k_B$. It is seen in Fig. 10 that the asymptotic value of BTE predictions at infinity agrees with the KTG predictions very well.

To manifest the effects of the internal heat capacity of molecules on the maximum evaporation flux, we also include in Fig. 10 the MD, BTE, and KTG results for the case of evaporation of LJ model Ar ($c_{V,int} = 0$) at $T_L = 82.8$ K into a vacuum. The fluid properties of the model Ar including the saturated density ($\rho_g = 0.142$ mol/L), the MAC ($\alpha = 0.92$), and the molecular collision frequency ($1/\tau$) are all taken from our previous MD studies [11,37]. For L_{vac} below 203 nm, the evaporation flux of the model Ar obtained directly from MD simulations [11] verifies the BTE prediction as shown in Fig. 10(b). With $\alpha = 0.92$ and $c_{V,int} = 0$, our KTG-based analysis predicts $v_{R,0} = 0.508$ and $J_{R,max} = 0.782$ in the limit of $L_{vac} \to \infty$. These two values are considerably higher than those for the fluid with $c_{V,int} = 31.5\,k_B$. In Fig. 10, we show that the KTG predictions of $v_{R,0}$ and $J_{R,max}$ for the monatomic fluid are also in good agreement with the asymptotic value of BTE predictions at infinity. Therefore, our modeling results clearly show that the dimensionless maximum evaporation flux $J_{R,max}$ is affected by the internal heat capacity of molecules.

D. Properties of the isotropic vapor

To further verify the KTG predictions about the properties of the isotropic vapor far from the evaporating surface (see Table II), we set $L_{vac} = 2000$ nm and solve the BTE for the dimensionless vapor temperature and density, i.e., T_x/T_L, T_y/T_L, $\rho_v/\rho_g(T_L)$, and the dimensionless vapor flow speed v_R along the evaporating vapor as shown in Fig. 11. We first use the temperature profiles in Fig. 11(a) to identify the region where the vapor can be considered isotropic. Near the evaporating surface, the vapor is highly anisotropic, and T_x and T_y approach each other in the vapor flow direction due to molecular collisions. Since the calculated mean free path of the Ar vapor molecules [11] are shorter than that of the model *n*-dodecane molecules, it is seen in Fig. 11(a) that T_x and T_y of the model Ar approach each other faster than *n*-dodecane. However, T_x of vapor is never exactly the same as T_y in Fig. 11(a), which means we still do not have an exact isotropic vapor region due to the finite L_{vac} in the model. To have an exact isotropic vapor, one needs to set $L_{vac} = \infty$. Hence, in Fig. 11(a) we consider the vapor region where T_x and T_y have the smallest difference as the approximate isotropic vapor. For the model *n*-dodecane and Ar, the minimum temperature difference is found at $x \approx 1030$ nm and $x \approx 1100$ nm, respectively. After the minimum temperature difference is reached, the temperature profiles split again and the vapor becomes more anisotropic as it approaches the vacuum boundary.

In Fig. 11(a), we show that the dimensionless temperature of the approximate isotropic vapor *n*-dodecane and the approximate isotropic vapor Ar is 0.971 ± 0.005 and 0.633 ± 0.001, respectively. These BTE predictions are in good agreement with $T_{R,1} = 0.975$ ($c_{V,int} = 31.5\,k_B$) and $T_{R,1} = 0.633$ ($c_{V,int} = 0$) predicted by the KTG model (see Table II).

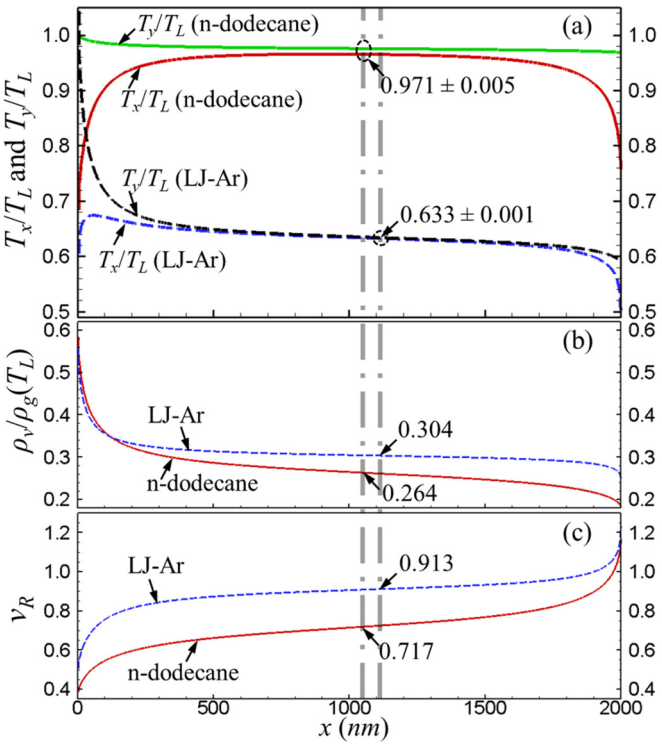

FIG. 11. The BTE predictions of (a) $T_{x,R}$, $T_{y,R}$, (b) ρ_R, and (c) v_R profiles in the evaporating vapor. The solid lines are results for the model *n*-dodecane. The dashed lines are results for the model Ar. The two vertical dash-dot lines indicate the position of approximate isotropic vapor for the model *n*-dodecane and the model Ar.

Similarly, we find from Fig. 11(b) that the dimensionless density of the approximate isotropic vapor *n*-dodecane and the approximate isotropic vapor Ar is 0.264 and 0.304, respectively. These values are consistent with $\rho_{R,1} = 0.262$ ($c_{V,\text{int}} = 31.5\,k_B, \alpha = 0.85$) and $\rho_{R,1} = 0.304$ ($c_{V,\text{int}} = 0, \alpha = 0.92$) predicted by the KTG model. Using the KTG-based analysis, we show in Sec. II C 2 that the isotropic vapor far from the evaporating surface moves at its speed of sound. Accordingly, the KTG prediction of the dimensionless flow speed in the isotropic vapor is $v_{R,1} = 0.718$ for the model *n*-dodecane ($c_{V,\text{int}} = 31.5\,k_B$) and $v_{R,1} = 0.913$ for the model Ar ($c_{V,\text{int}} = 0$). These values agree with $v_{R,1} = 0.717$ for the model *n*-dodecane and $v_{R,1} = 0.913$ for the model Ar shown in Fig. 11(c), which also verifies that the isotropic vapor moves at its speed of sound. All of the above results verify that the internal heat capacity of molecules will affect the properties of the isotropic vapor far from the evaporating surface when the maximum evaporation flux is reached.

E. Why does $J_{R,\max}$ decrease with increasing $c_{V,\text{int}}$?

The BTE solution shown in Fig. 11 also provide insights into why $J_{R,\max}$ is dependent on $c_{V,\text{int}}$. After the emitted molecules leave the evaporating surface, a portion of them will return to the surface and condense due to the molecular collisions in vapor as they travel towards the vacuum boundary. The percentage of the outgoing molecules that return to liquid surface is related to the distribution of v_x of vapor molecules (see, e.g., Fig. 5). As the portion of vapor molecules with $v_x < 0$ increases, a higher percentage of vapor molecules tend to return to the surface, and thus the $J_{R,\max}$ becomes smaller. Figure 11(a) shows that the molecular collisions bring T_x and T_y (or T_{int} since $T_y \approx T_{\text{int}}$) closer to each other in the vapor flow direction. For vapors with a higher $c_{V,\text{int}}$ such as the model *n*-dodecane, the increase in T_x/T_L due to molecular collisions is more significant than that in vapors with a lower $c_{V,\text{int}}$ such as Ar [see Fig. 11(a)]. A higher T_x in the evaporating vapor means a broader distribution of v_x. As the shifted Maxwell distribution becomes broader, the portion of vapor molecules with $v_x < 0$ increases and a higher percentage of vapor molecules will return to the surface and condense, which results in a smaller $J_{R,\max}$. Moreover, as T_x increases, the normal pressure in the vapor near the evaporating surface will also increase and become closer to the saturated pressure. The smaller pressure difference between the saturated pressure and the pressure in vapor also leads to a smaller $J_{R,\max}$.

VI. CONCLUSIONS

Using the combination of KTG-based analysis, the BTE, and the MD simulation, we study the process of evaporation of molecular fluids from a planar liquid surface into a vacuum. The MD simulation results validate the following key assumptions in the theoretical analysis:

(1) The VDF of evaporating vapor molecules can be well approximated by the shifted anisotropic Maxwell distribution given by Eq. (6).

(2) The temperature of molecular internal motions (T_{int}) is approximately equal to that of molecular translational motions perpendicular to vapor flow direction (T_y) in the nonequilibrium evaporating vapor.

(3) The collision term in the BTE can be well approximated by the BGK approximation for nonequilibrium evaporating vapor molecules.

With these assumptions, we study the effects of molecular internal motions ($c_{V,\text{int}}$), the MAC (α), and the distance between evaporating surface and vacuum boundary (L_{vac}) on the transport phenomena in the evaporating vapor.

While our modeling results show that the dimensionless maximum evaporation flux $J_{R,\max}$ depends on $c_{V,\text{int}}$, α, and L_{vac}, there are several universal features of the evaporating vapor which are independent of $c_{V,\text{int}}$, α, and L_{vac}. These features include the following:

(1) T_y and ρ_v will decrease monotonically in the evaporating vapor flow direction, and the vapor flow speed (v_a) will increase monotonically in the vapor flow direction.

(2) T_x of the evaporating vapor will reach the maximum value at the position where $v_R = \sqrt{0.5}$. If v_R is less than $\sqrt{0.5}$, T_x will increase in the vapor flow direction. If v_R is greater than $\sqrt{0.5}$, T_x will decrease in the vapor flow direction.

(3) v_R of the evaporating vapor will reach the maximum value $\sqrt{1.5}$ at the vacuum boundary.

(4) If the vacuum boundary is far from the evaporating surface, the evaporating molecules will have sufficient time to collide with one another such that the vapor becomes isotropic before it reaches the vacuum boundary. In this case, the isotropic vapor moves at its speed of sound regardless of whether it is a monatomic vapor or polyatomic vapor.

These features are all verified by our MD simulation results and the BTE solutions. They also agree with the existing experimental results. In the limit of $L_{\text{vac}} \to \infty$, the dimensionless maximum evaporation flux ($J_{R,\max}$) and the properties of isotropic vapor far from the evaporating surface are predicted by the KTG-based analysis. The KTG predictions shown in Tables I and II are partially validated by the combination of MD simulation and the BTE solution on the evaporation of the model Ar and the model *n*-dodecane into a vacuum.

Finally, we want to point out that all theoretical predictions from this work are based on the several assumptions made in the theoretical model. If the key assumptions such as the shifted Maxwellian VDFs and the BKG approximation of the collision term are found inexact for other model fluids or real fluid systems, the speculations from our theoretical model could be inaccurate. Therefore, it is imperative in the future to further verify these assumptions and theoretical predictions with other fluids in experiment or by MD simulations.

ACKNOWLEDGMENTS

This work was supported by NSF CBET Thermal Transport Processes Program under Grant No. 1911433. Additionally, we would like to thank the eXtreme Science and Engineering Discovery Environment (XSEDE) for providing us supercomputer resources for MD simulations.

APPENDIX: DERIVATIONS OF EQS. (23) AND (24), AND THE CALCULATION OF $T_{R,1}$ AND $\rho_{R,1}$

1. Derivation of Eq. (23)

Dividing Eq. (16) by Eq. (21), we directly obtain Eq. (23a). Substituting Eq. (23a) into Eq. (16), we obtain Eq. (23c). Substituting Eq. (23a) and (23c) into Eq. (22), we have

$$\alpha = \frac{\alpha/2}{\Gamma(v_{R,0}) - (1-\alpha)\Gamma(-v_{R,0})}\left[T_{x,R}\mathrm{E}(v_{R,0})\Big/\left(1 + \frac{\bar{E}_{\text{int}}(T_L)}{2k_BT_L}\right) - 2(1-\alpha)\Gamma(-v_{R,0})\right]. \tag{A1}$$

Rearranging Eq. (A1), we obtain

$$2\left(1 + \frac{\bar{E}_{\text{int}}(T_L)}{2k_BT_L}\right)\Gamma(v_{R,0}) = T_{x,R}\mathrm{E}(v_{R,0}). \tag{A2}$$

Substituting the expression of $E(v_{R,0})$ [i.e., Eq. (9c)] into Eq. (A2), we obtain

$$\left(2 + \frac{\bar{E}_{\text{int}}(T_L)}{k_BT_L}\right)\Gamma(v_{R,0}) = T_{x,R}\sqrt{\pi}\,v_{R,0}\Phi(v_{R,0}) + \left(T_{x,R} + T_{y,R} + \frac{\bar{E}_{\text{int}}(T_{\text{int},0})}{k_BT_L}\right)\Gamma(v_{R,0}). \tag{A3}$$

Using the assumption of $T_{\text{int},0} = T_{y,0}$ and rearranging Eq. (A3), we obtain

$$\left(2 + \frac{\bar{E}_{\text{int}}(T_L) - \bar{E}_{\text{int}}(T_{y,0})}{k_BT_L} - T_{x,R} - T_{y,R}\right)\Gamma(v_{R,0}) = T_{x,R}\sqrt{\pi}\,v_{R,0}\Phi(v_{R,0}). \tag{A4}$$

In Eq. (A4), $\bar{E}_{\text{int}}(T_L) - \bar{E}_{\text{int}}(T_{y,0}) = c_{V,\text{int}}(T_L - T_{y,0})$ where $c_{V,\text{int}}$ is evaluated at a temperature between $T_{y,0}$ and T_{L}. Therefore, we have

$$\left[2 + \frac{c_{V,\text{int}}}{k_B} - T_{x,R} - \left(\frac{c_{V,\text{int}}}{k_B} + 1\right)T_{y,R}\right]\Gamma(v_{R,0}) = T_{x,R}\sqrt{\pi}\,v_{R,0}\Phi(v_{R,0}). \tag{A5}$$

From Eq. (A5), we obtain the expression for $T_{y,R}$:

$$T_{y,R} = \left(2 + \frac{c_{V,\text{int}}}{k_B} - T_{x,R} - \frac{T_{x,R}\sqrt{\pi}\,v_{R,0}\Phi(v_{R,0})}{\Gamma(v_{R,0})}\right)\Big/\left(\frac{c_{V,\text{int}}}{k_B} + 1\right). \tag{A6}$$

Substituting the expression for $T_{x,R}$ [i.e., Eq. (23a)] into Eq. (A6), we finally obtain

$$T_{y,R} = 1 + \left(1 - \left[\frac{\Gamma(v_{R,0})}{2\Phi(v_{R,0})}\right]^2 - \frac{\Gamma(v_{R,0})\sqrt{\pi}\,v_{R,0}}{4\Phi(v_{R,0})}\right)\Big/\left(\frac{c_{V,\text{int}}}{k_B} + 1\right). \tag{A7}$$

2. Derivation of Eq. (24)

The net molar flux from the evaporating surface can be calculated by $J_{\text{net},x=0} = \rho_{v,0}v_{a,0}$, where $\rho_{v,0}$ and $v_{a,0}$ are the density and macroscopic speed of vapor at the vapor side of the liquid-vapor interface. Accordingly, the dimensionless evaporation molar flux is defined as (J_R), which is defined as the ratio of $J_{\text{net},x=0}$ to $J_L{}^+$, given by

$$J_R = \frac{\rho_{v,0}v_{a,0}}{\rho_g(T_L)\sqrt{\frac{k_BT_L}{2\pi m}}} = 2\rho_R\sqrt{T_{x,R}}\sqrt{\pi}\,v_{R,0}. \tag{A8}$$

Substituting the expression for ρ_R [i.e., Eq. (23c)] and the expression for $T_{x,R}$ [i.e., Eq. (23a)] into Eq. (A8), we obtain

$$J_R = \frac{2\sqrt{\pi}\alpha\,v_{R,0}}{\Gamma(v_{R,0}) - (1-\alpha)\Gamma(-v_{R,0})}. \tag{A9}$$

3. Calculation of $T_{R,1}$ and $\rho_{R,1}$

To find $T_{R,1}$ ($T_{R,1} = T_1/T_L$), we apply Eq. (28) in the maximum evaporation case:

$$\tfrac{1}{2}mv_{a,0,\max}^2 + \tfrac{3}{2}k_BT_{x,0} + k_BT_{y,0} + c_{V,\text{int}}T_{y,0} = \tfrac{1}{2}mv_{a,1,\max}^2 + \tfrac{5}{2}k_BT_1 + c_{V,\text{int}}T_1. \tag{A10}$$

Using the definition $v_{R,0} = v_{a,0}/\sqrt{2k_BT_{x,0}/m}$ and $v_{R,1} = v_{a,1}/\sqrt{2k_BT_1/m}$, Eq. (A10) becomes

$$k_BT_{x,0}\Big[v_{R,0,\max}^2 + \frac{3}{2} + \Big(1 + \frac{c_{V,\text{int}}}{k_B}\Big)T_{R,0}\Big] = k_BT_1\Big(v_{R,1,\max}^2 + \frac{5}{2} + \frac{c_{V,\text{int}}}{k_B}\Big), \tag{A11}$$

where $T_{R,0} = T_{y,0}/T_{x,0}$. Dividing both sides of Eq. (A11) by k_BT_L, we obtain

$$T_{x,R}\Big[v_{R,0,\max}^2 + \frac{3}{2} + \Big(1 + \frac{c_{V,\text{int}}}{k_B}\Big)T_{R,0}\Big] = T_{R,1}\Big(v_{R,1,\max}^2 + \frac{5}{2} + \frac{c_{V,\text{int}}}{k_B}\Big). \tag{A12}$$

Rearranging Eq. (A12), we get

$$T_{R,1} = \frac{T_{x,R}\big(v_{R,0,\max}^2 + \frac{3}{2}\big) + \big(1 + \frac{c_{V,\text{int}}}{k_B}\big)T_{y,R}}{v_{R,1,\max}^2 + \frac{5}{2} + \frac{c_{V,\text{int}}}{k_B}}. \tag{A13}$$

In Eq. (A13), $v_{R,0,\max}$ is given in Table I, and $v_{R,1,\max}$ is given by Eq. (34). Plugging the $v_{R,0,\max}$ value into Eqs. (23a) and (23b), we obtain $T_{x,R}$ and $T_{y,R}$ in Eq. (A13). We thus obtain $T_{R,1}$.

To find $\rho_{R,1}[\rho_{R,1} = \rho_{v,1}/\rho_g(T_L)]$, we use the definition of $J_{R,\max}$:

$$J_{R,\max} = \frac{\rho_{v,1}v_{a,1,\max}}{\rho_g(T_L)\sqrt{\frac{k_BT_L}{2\pi m}}}. \tag{A14}$$

Rearranging Eq. (A14), we obtain

$$J_{R,\max} = 2\rho_{R,1}\sqrt{\pi T_{R,1}}v_{R,1,\max}. \tag{A15}$$

Hence,

$$\rho_{R,1} = \frac{J_{R,\max}}{2\sqrt{\pi T_{R,1}}v_{R,1,\max}}. \tag{A16}$$

Using the values of $T_{R,1}$, $v_{R,1,\max}$, and $J_{R,\max}$ found in the previous calculations, we will find $\rho_{R,1}$.

[1] M. Chaker and C. B. Meher-Homji, Gas turbine power augmentation: Parametric study relating to fog droplet size and its influence on evaporative efficiency, J. Eng. Gas Turbines Power **133**, 092001 (2011).

[2] R. Tao, K. Huang, H. Tang, and D. Bell, Electrorheology leads to efficient combustion, Energy Fuels **22**, 3785 (2008).

[3] T. Lim, S. Han, J. Chung, J. T. Chung, S. Ko, and C. P. Grigoropoulos, Experimental study on spreading and evaporation of inkjet printed pico-liter droplet on a heated substrate, Int. J. Heat Mass Transfer **52**, 431 (2009).

[4] J.-U. Park, M. Hardy, S. J. Kang, K. Barton, K. Adair, D. K. Mukhopadhyay, C. Y. Lee, M. S. Strano, A. G. Alleyne, J. G. Georgiadis, P. M. Ferreira, and J. A. Rogers, High-resolution electrohydrodynamic jet printing, Nat. Mater. **6**, 782 (2007).

[5] A. H. Persad and C. A. Ward, Expressions for the evaporation and condensation in the Hertz-Knudsen relation, Chem. Rev. **116**, 7727 (2016).

[6] T. Ytrehus and S. Østmo, Kinetic theory approach to interphase processes, Int. J. Multiphase Flow **22**, 133 (1996).

[7] P. D. Crout, An application of kinetic theory to the problems of evaporation and sublimation of monatomic gases, J. Math. Phys. **15**, 1 (1936).

[8] R. Mager, G. Adomeit, and G. Wortberg, Theoretical and experimental investigation of strong evaporation of solids, in *Rarefied Gas Dynamics,* edited by E. P. Muntz, D. P. Weaver, and D. H. Campbell (AIAA, Washington, DC,1989), pp. 460–469.

[9] D. A. Labuntsov and A. P. Kryukov, Analysis of intensive evaporation and condensation, Int. J. Heat Mass. Transfer **22**, 989 (1979).

[10] J. Fischer, Distribution of pure vapor between two parallel plates under the influence of strong evaporation and condensation, Phys. Fluids **19**, 1305 (1976).

[11] E. Bird and Z. Liang, Transport phenomena in the Knudsen layer near an evaporating surface, Phys. Rev. E **100**, 043108 (2019).

[12] J. Safarian and T. A. Engh, Vacuum evaporation of pure metals, metal, Metal. Mater. Trans. A **44**, 747 (2013).

[13] M. Kon, K. Kobayashi, and M. Watanabe, Liquid temperature dependence of kinetic boundary condition at vapor–liquid interface, Int. J. Heat Mass Transfer **99**, 317 (2016).

[14] R. Hołyst and M. Litniewski, Evaporation into vacuum: Mass flux from momentum flux and the Hertz-Knudsen relation revisited, J. Chem. Phys. **130**, 074707 (2009).

[15] T. Ishiyama, T. Yano, and S. Fujikawa, Molecular dynamics study of kinetic boundary condition at an interface between argon vapor and its condensed phase, Phys. Fluids **16**, 2899 (2004).

[16] V. V. Zhakhovsky, A. P. Kryukov, V. Y. Levashov, I. N. Shishkova, and S. I. Anisimov, Mass and heat transfer between

evaporation and condensation surfaces: Atomistic simulation and solution of Boltzmann kinetic equation, Proc. Natl. Acad. Sci. USA **116**, 18209 (2019).

[17] T. Ishiyama, T. Yano, and S. Fujikawa, Kinetic Boundary Condition at a Vapor-Liquid Interface, Phys. Rev. Lett. **95**, 084504 (2005).

[18] R. Meland, Molecular dynamics simulation of the inverted temperature gradient phenomenon, Phys. Fluids **15**, 3244 (2003).

[19] R. W. Schrage, *A Theoretical Study of Interphase Mass Transfer* (Columbia University Press, New York, 1953).

[20] V. P. Carey, *Liquid–Vapor Phase-Change Phenomena* (Hemisphere, New York, 1992).

[21] Y. Sone, *Molecular Gas Dynamics* (Birkhauser, Boston, 2007).

[22] J. Gonzalez, J. Ortega, and Z. Liang, Prediction of thermal conductance at liquid-gas interfaces using molecular dynamics simulations, Int. J. Heat Mass Transfer **126**, 1183 (2018).

[23] E. Bird, J. Gutierrez-Plascencia, and Z. Liang, Thermal transport across the interface between liquid n-dodecane and its own vapor: A molecular dynamics study, J. Chem. Phys. **152**, 184701 (2020).

[24] S. K. Nath, F. A. Escobedo, and J. J. de Pablo, On the simulation of vapor–liquid equilibria for alkanes, J. Chem. Phys. **108**, 9905 (1998).

[25] R. Khare, J. J. de Pablo, and A. Yethiraj, Rheological, thermodynamic, and structural studies of linear and branched alkanes under shear, J. Chem. Phys. **107**, 6956 (1997).

[26] S. H. Pine, *Organic Chemistry*, 2nd ed. (McGraw-Hill, New York, 1964).

[27] P. Padilla and S. Toxvaerd, Self-diffusion in *n*-alkane fluid models, J. Chem. Phys. **94**, 5650 (1991).

[28] W. L. Jorgensen, J. D. Madura, and C. J. Swenson, Optimized intermolecular potential functions for liquid hydrocarbons, J. Am. Chem. Soc. **106**, 6638 (1984).

[29] B. Smit, S. Karaborni, and J. I. Siepmann, Computer simulations of vapour liquid phase equilibria of n-alkanes, J. Chem. Phys. **102**, 2126 (1995).

[30] D. Frenkel and B. Smit, *Understanding Molecular Simulation* (Springer, Berlin, 2002).

[31] S. M. Foiles, M. I. Baskes, and M. S. Daw, Embedded-atom-method functions for the fcc metals Cu, Ag, Au, Ni, Pd, Pt, and their alloys, Phys. Rev. B **33**, 7983 (1986).

[32] A. K. Rappe, C. J. Casewit, K. S. Colwell, W. A. Goddard, and W. M. Skiff, UFF, a full periodic table force field for molecular mechanics and molecular dynamics simulations, J. Am. Chem. Soc. **114**, 10024 (1992).

[33] P. L. Bhatnagar, E. P. Gross, and M. Krook, A model for collision processes in gases. I. small amplitude processes in charged and neutral one-component systems, Phys. Rev. **94**, 511 (1953).

[34] Donald A. McQuarrie and John D. Simon, *Molecular Thermodynamics* (University Science Books, Sausalito, CA, 1999).

[35] S. Chandrasekhar, Rev. Mod. Phys. **15**, 1 (1943).

[36] M. P. Allen and D. J. Tildesley, *Computer Simulation of Liquids* (Clarendon, Oxford, 2000).

[37] Z. Liang, T. Biben, and P. Keblinski, Molecular simulation of steady-state evaporation and condensation: Validity of the Schrage relationships, Int. J. Heat Mass Transfer **114**, 105 (2017).